ESI Continuation Review

Grant Performance Summary

NASA Grant Number 21-ESI-0049

11/25/2022

Advanced Lightweight Heat Rejection Radiators for Space Nuclear Power Systems

University of New Mexico's Institute for Space and Nuclear Power Studies (UNM-ISNPS) and Nuclear Engineering Department

Principal Investigator	Distinguished and Regents' Professor Mohamed S. El-Genk, UNM-ISNPS and NE Dept.
NASA Research Collaborator	NASA RC Fernando Reyes Tirado, MSFC

1. RESEARCH OBJECTIVES

The objectives of the NASA Early Stages Innovation (ESI) award to the University of New Mexico's Institute for Space and Nuclear Power Studies (UNM-ISNPS) are to: (a) to develop a lightweight and foldable heat pipes radiator panel for heat rejection at surface temperatures from 500 – 600 K with a specific mass ≤ 3 kg/m^2, and (b) advance the TRL of the innovative advanced heat pipe radiator concept proposed with technologies to enhance heat rejection, reduce mass, and decrease secondary loop pumping requirements requires both design optimization, simulation and modeling analyses, and experimental research.

The foci of this research effort at UNM-ISNPS are to: (a) develop and optimize design of an advanced lightweight heat pipes radiator panel concept using thermal and structural modeling and simulation analyses, and (b) investigate methods of diffusion bonding and characterize interfaces for the HOPG/Ti/C-C and Ti/C-C composite structures. The research completed during the first year includes:

- Selecting a heat pipe working fluid and structural materials for the temperature range of interest, performing parametric analyses to determine the operation limits and power throughput of Ti/Cs and Ti/Rb heat pipes, and selecting the heat pipe cross-section to ensure that the vapor flow for operating at 500 – 600 K heat rejection temperature, is in the continuum flow regime.
- Developing a lumped parameter thermal model of the heat pipe radiator module for performing parametric and design optimization analyses of effects of the dimensions of the heat pipes, HOPG/Ti/C-C fins, and NaK-78 duct on the radiator performance and areal density.
- Developing CFD thermal-hydraulic model of a heat pipe module to determine the effects of the material selection and dimensions and the thermal coupling of the heat pipes to the flowing alkali-metal liquid in the header duct of the modular for achieving an average surface temperature ranging from 500 – 600 K.
- Conducting 3-D computational fluid Dynamics (CFD) analyses to investigate methods of thermal coupling of the heat pipes to the composite HOPG/Ti/C-C heat spreading fins and the investigate the effects of the surface temperature and geometry on the areal density of the radiator modules.
- Investigating methods to develop diffusion bonding at the Ti/HOPG and Ti/C-C composite interfaces. Samples of Ti coated C-C composite and HOPG are coated with thin layers of Ti using magnetron sputtering and interfaces are characterized using SEM and FIB techniques.

2. INTRODUCTION AND BACKGROUND

Nuclear reactor power and propulsion systems are enabling of future NASA missions of space and planetary explorations including crewed missions to the Moon and Mars. The nuclear electric and thermal propulsion options effectively decrease transit time reducing the astronauts' exposure to the hazardous space ionizing radiation and the energetic galactic cosmic rays. To reduce the launch cost and stowed volume and mass they require light weight radiators to reject waste heat into space. The heat rejection radiators of nuclear reactor power systems are one of the most voluminous and massive components of the system. Figure 1 shows a schematic of a space reactor power system with a conical heat rejection radiator consisting of 6 fixed and 12 deployable heat pipe panels.

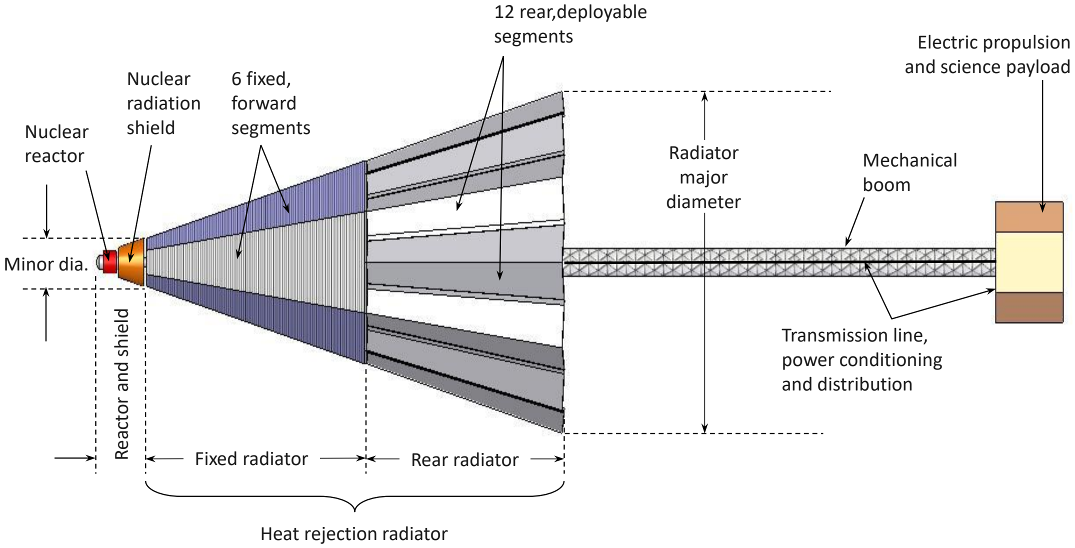

Figure 1: Schematic of a space nuclear reactor power system with a conical heat pipe heat rejection radiator [1].

NASA has outlined design goals for advanced heat pipe radiators that are much lighter than current State-of-the-Art (SOA) and reject waste heat at surface temperatures of ~500 - 600 K for up to 10 years (Table 1) [2]. In addition, the advanced radiators should operate both in microgravity and in low gravity environments, such as on the surface of the Moon, and be sufficiently strong to survive launch vibration loads and space environmental hazards including micrometeoroids, atomic oxygen erosion, energetic ionizing solar radiation, and high energy gamma and neutrons emanated from nuclear reactor.

Table 1. Design requirements and desirable characteristics for radiator concept**.**

• Nominal heat rejection at temperatures between 500 – 600 K.
• Integrated radiator aerial density ≤ 3 kg/m^2 including all major radiator components.
• Operate in microgravity, low gravity, and high thrust environments.
• Operation service life ≥ 10 years.
• Modular, deployable, and capable of surviving vibration loading during launch, landing, and deployment.
• Survive environmental hazards such as micrometeoroid impacts, solar UV radiation, ionizing radiation from the nuclear reactor, and atomic oxygen erosion in Earth orbit.

State-of-the-Art (SOA) heat rejection radiator designs developed for space nuclear reactor power systems [1,3-9] are compared in Fig. 2. This figure compares the reported values of the radiator areal density (or specific mass) in kg/m^2 versus the projected average surface temperatures. The space nuclear power systems with dynamic energy conversions using Closed Brayton Cycle (CBC) single shaft turbomachinery and Free Piston Stirling Engine (FPSE) operate at high thermal efficiencies > 20% and low reactor thermal power and smaller masses of the reactor and the radiation shadow shield. However, the rejected waste heat at low temperatures < 500 K increases the surface area and the corresponding areal density of the radiator [3-6].

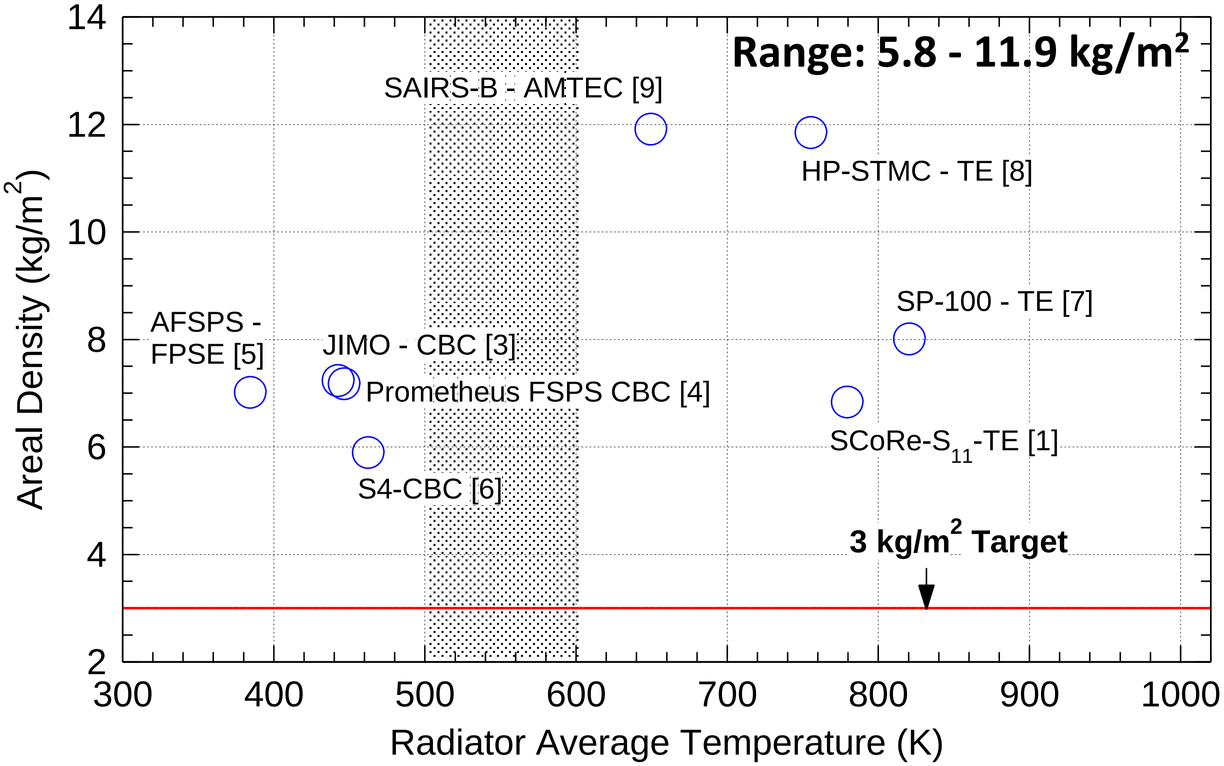

Figure 2: Comparison of reported areal densities of State-of-the-Art (SOA) heat rejection radiator designs for space nuclear power systems.

Conversely, the space nuclear reactor power systems employing static thermoelectric (TE) energy conversion operate at lower thermal efficiency (5% - 15%) but reject the waste heat at higher radiator temperatures (700- 800 K). Thus, depending on the thermal efficiency of the power system, such high surface temperatures decrease the size and mass of the heat rejection radiator. The SP-100, and SCoRe-S_{11}-TE nuclear reactor power systems used SiGe TE elements for energy conversion [1, 7] and HP-STMC power system used higher-efficiency segmented Skutterudite TE elements for partially converting the reactor thermal power to DC electricity [8].

The SAIRS-B space nuclear reactor power system with static sodium Alkali Metal Thermal to Electric Conversion (AMTEC) has a thermal efficiency comparable to those of the dynamic conversion options but at higher radiator surface temperature [9]. AMTEC converters operate at the highest fraction of Carnot of any static or dynamic conversion technologies [10] but are currently at a low Technology Readiness Level (TRL). Thus, for the same electrical power of the power system, thermal power of the reactor, and the masses and sizes of the reactor and the radiation shadow shield would be lower. In addition, the surface area and the areal density of radiator are lower than with either TE or dynamic energy conversion options.

At average surface temperature ≤ 500 K, reported estimate of the areal densities for waste heat rejection radiators into space with Ti-water heat pipe panels ranges from 5.8 kg/m^2 for the S^4-CBC system to 7.16 kg/m^2 for the Prometheus JIMO mission [3-6]. These water heat pipe radiator designs use heat spreading fins made of lightweight C-C composites or aluminum. The radiator designs for systems with static energy conversion and higher heat rejection temperatures have estimated areal densities of 6.82 – 11.9 kg/m^2. The radiators for the SP-100 reference design, the SCoRe-S$_{11}$, SAIRS-B, and HP-STMC nuclear reactor power systems employ titanium heat pipes with potassium or rubidium working fluids [1,7-9].

The armor to protect heat pipes from impacts by micrometeorites and space debris can add as much as 30% - 50% to the radiator mass and areal density (Fig. 2). This has been the case for the SP-100, SAIRS-B, and heat pipe-STMC nuclear reactor power system designs. On the other hand, the protective armor of the radiator surface and the heat pipes increases reliability for long operation missions (7-10 years), at the expense of increasing the areal density. Some of the SOA radiator designs in Figure 2 for operating at temperatures below and above the 500 – 600 K targeted by NASA for this project have areal densities of 5.8-11.9 kg/m^2. These are well above the NASA desired ≤ 3 kg/m^2.

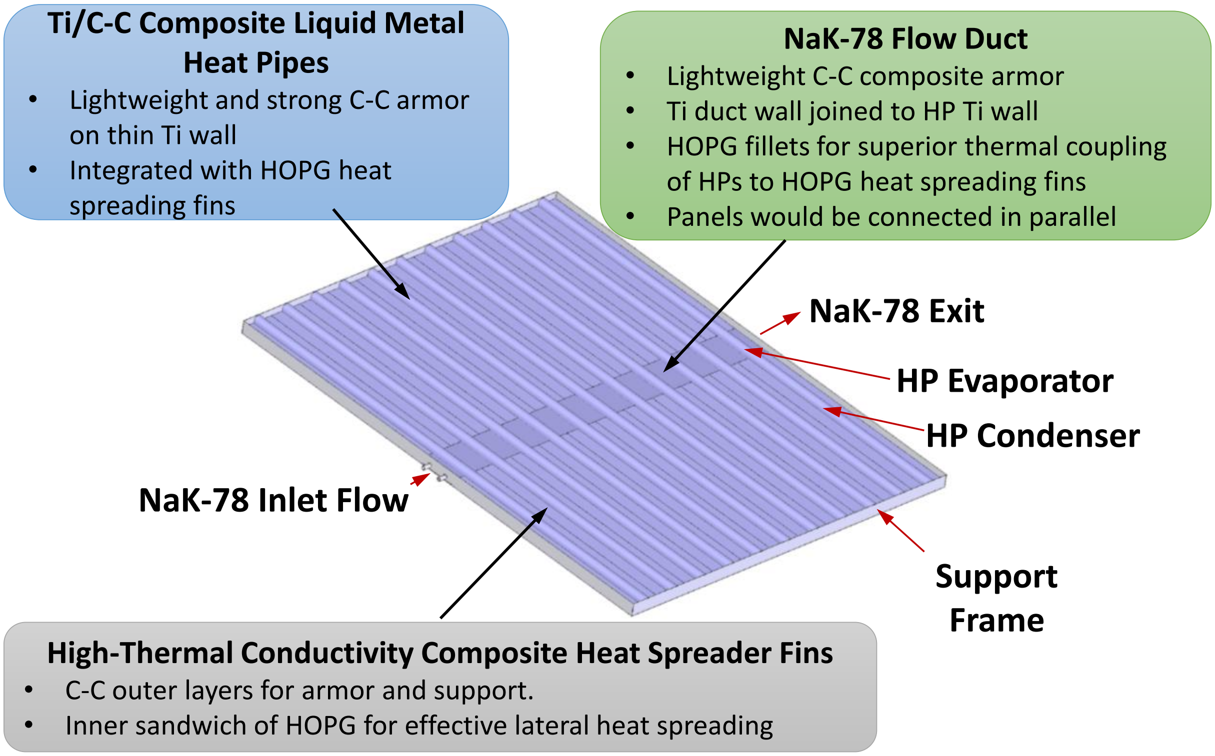
Ti/C-C Composite Liquid Metal Heat Pipes
- Lightweight and strong C-C armor on thin Ti wall
- Integrated with HOPG heat spreading fins

NaK-78 Flow Duct
- Lightweight C-C composite armor
- Ti duct wall joined to HP Ti wall
- HOPG fillets for superior thermal coupling of HPs to HOPG heat spreading fins
- Panels would be connected in parallel

High-Thermal Conductivity Composite Heat Spreader Fins
- C-C outer layers for armor and support.
- Inner sandwich of HOPG for effective lateral heat spreading

Figure 3: Developed lightweight heat pipe radiator panel concept for waste heat rejection.

3. DEVELOPED ADVANCED LIGHTWEIGHT RADIATOR CONCEPTS

The advanced lightweight heat pipe radiator panel design concepts developed in this research provide notable advantages compared to the SOA (Fig. 2). Figure 3 presents a layout of one of two developed heat pipe radiator panel concept. The rectangular panels would be folded up for storage during launch and deployed in a scissor-arrangement prior to startup of the space nuclear reactor power system. The identical rectangular panels are hydraulically coupled in parallel to the power system's heat rejection loop for the same inlet and outlet temperatures of the working fluid for water heat rejection. Each panel comprises of heat pipe modules with HOPG/Ti/C-C heat spreading fins with a shared liquid NaK-78 duct.

3.1. Developed Designs of Advanced and lightweight Heat Rejection Radiator Modules

Table 2 lists the properties for the selected structural materials for the lightweight radiator panel design. The NaK-78 liquid eutectic has a low melting point of 260.6 K, density < ~ 867 kg/m^3, and estimated boiling temperature at atmospheric pressure of 1058 K [11]. In addition to liquid NaK flow duct, each heat rejection radiator module in the panel with a Ti-Cs heat pipe has a 'double ended' configuration (Figs. 4 - 7). The middle evaporator section of the heat pipe is thermally coupled to the liquid NaK flow and to two equal length condenser sections on each side. The heat pipes with thin 0.2 mm thick Titanium (Ti) wall and porous wick are covered with 1.0 mm thick C-C composite armor for protection against impacts by micrometeoroids and space debris (Table 2). Titanium for the heat pipe wall and porous wick has a low density of 4,510 kg/m^3, high ductility and tensile strength and melting temperature of 1,943 K. It also compatible with alkali metal working fluids and reported research results suggest it can be readily joined to C-C composites [12-15].

Table 2. Properties of Selected Materials for Developed Radiator Concept.

Materials	Density(kg/m^3)	Conductivity (W/m-K)	YS (MPa)	UTS (MPa)	Thickness (mm)
Titanium	4510	19.4	200	97	Ti: 0.1 - 0.2
C-C Armor	1400-1800	125 / 10	160	300-350	HP: 1.0 HOPG: 0.1 – 0.2
HOPG Fins	2200	1800 / 8	120	80	HOPG: 0.3 - 1
NaK-78	867	25	260 K (-12 °C) melting point		

The C-C composites with strong and flexible woven structure, have lower density than Ti (1,400 -1,800 kg/m^3), and can operate at elevated temperatures (Table 2) [15,16]. The woven carbon fibers within the C-C composites provide higher in-plane thermal conductivity to help the rejection of waste heat rejected from the surfaces of heat pipe and the HOPG/Ti/C-C heat spreading fins by radiation into space. The C-C composite armor has been widely used and considered by the US Department of Defense for protecting hypersonic reentry vehicles heat shields from impacts by space debris impacts [17]. The strong C-C armor also provides additional structural support to the Cs heat pipes. This armor continuous structural is laid onto the outside of the heat pipe and radiator fins. The one mm thick C-C armor for the heat pipes and NaK flow duct is half that of the heat spreading fins (0.2 mm thick) (Table 2).

3.1.1 Radiator Module Design Version 1

Figure 4a presents cutaway sectional views of one of the two developed designs of the radiator heat pipe modules showing the liquid NaK-78 header duct with the flow is normal to the image. Figure 4b is a cross sectional view showing the details of the heat pipe design and the Ti/HOPG/C-C composite heat spreading fins. The heat pipe is flat on one side, for good thermal contact with the liquid NaK-78 header duct wall and the HOPG/Ti/C-C heat spreading fins and is rounded on top for increased strength. The heat pipe 0.1 mm thick Ti porous wick is separated from the Ti wall by a liquid annulus for the flow of the working fluid condensate from the condenser to the heat pipe evaporator. The liquid flow through the annulus reduces the pressure losses for the liquid return from the condenser sections to the evaporator section of the heat pipes, but also raises the heat pipe wicking limit. An internal Ti web divider may be used, if needed, for structural strength to support the heat pipe wall during launch and to resist acoustic vibration of the stowed radiator panels within the rocket during launch.

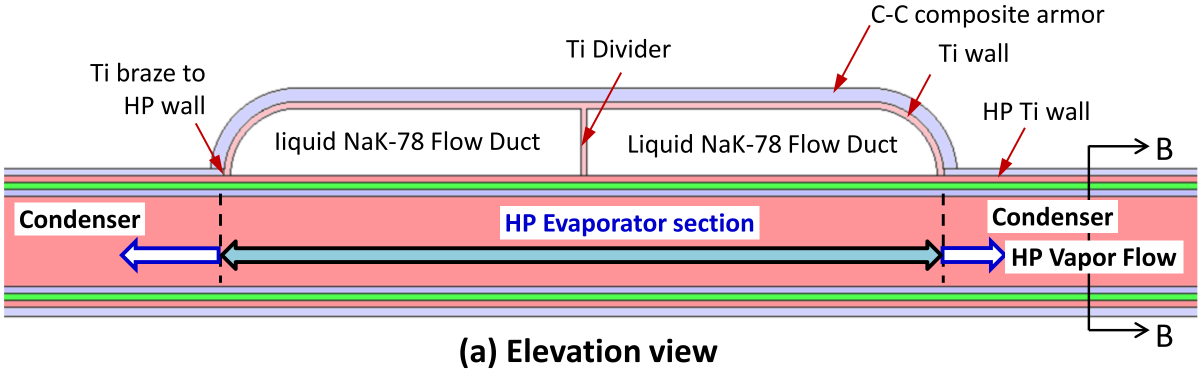

(a) Elevation view

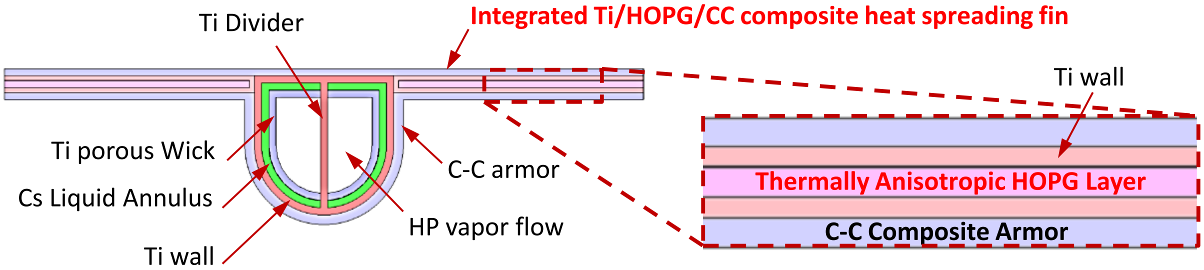

(b) Side view B-B

Figure 4: Sectional views of heat pipe radiator module design Version 1 in the panel concept in Fig. 3 showing the heat pipe internal structure, liquid NaK-78 flow duct, and composition of the layered HOPG/Ti/C-C composite waste heat spreading fins.

The composite HOPG/Ti/C-C heat spreading fins in Fig. 4 comprises a central layer of thermally anisotropic Highly Oriented Pyrolytic Graphite (HOPG) between thin layers of Ti. The HOPG is specialized graphite with graphene layers oriented in the same direction, which results in an extremely high in-plane thermal conductivity of 1,800-2,000 W/mK and low off-plane thermal conduction of 8 W/mK (Table 2) [18-19]. The HOPG in the heat spreading fins is oriented with its highest thermal conductivity is in the fins, conductively coupled to the perpendicular wall of the heat pipe, effectively spread the waste heat along the fins. This high lateral conductivity helps reduces the temperature drop along the fins and the variation is surface temperature for radiative heat rejection into space.

The HOPG/Ti/C-C heat spreading fins are joined and conductively coupled to the Ti heat pipe wall using HOPG curved fillets, as needed, to enhance the conduction coupling and decrease the heat pipe wall temperature while increase the surface average temperature of the heat spreading fins. Depending on the angle of fillets, q, they could add to the total mass of the modular, but the decreased thickness of the HOPG layer in the heat spreading fins, to attain surface average temperature of 500 - 600 K, may be decreased with the opposite effect on the modular mass. The exposed surfaces of the HOPG/Ti/C-C fins and the heat pipes are protected by a thin layer of C-C composite armor (Table 2). It has been experimentally demonstrated that thin layers of the C-C composite resist cracking by hypervelocity impacts simulating those by micrometeorites and space debris [20]. The HOPG, Ti, and C-C composite layers in the heat spreading fins are thought to be joined strongly together with diffusion bonding at the comment interfaces to support long operation life of ≥ 10 years. Investigating and characterizing diffusion bonding between the Ti and C-C layers and Ti and HOPG layers is a key focus of the research conducted during the first year of the award, and which are detailed later in section 8 of this report.

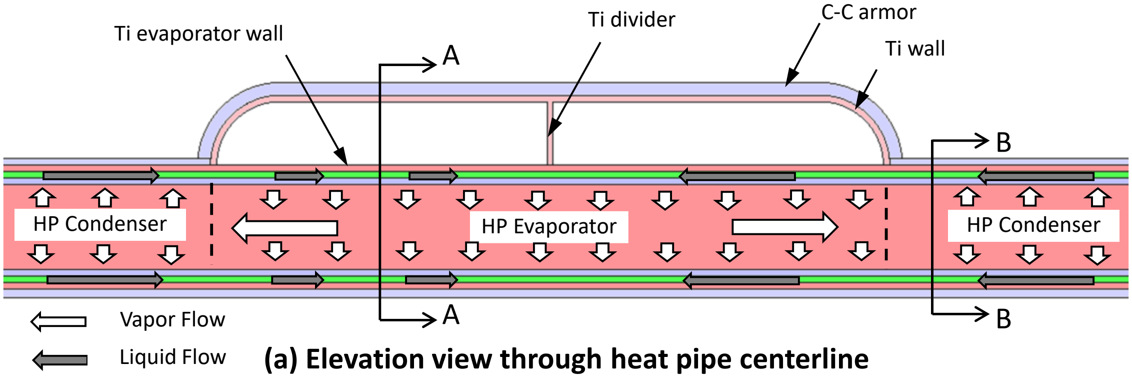

(a) Elevation view through heat pipe centerline

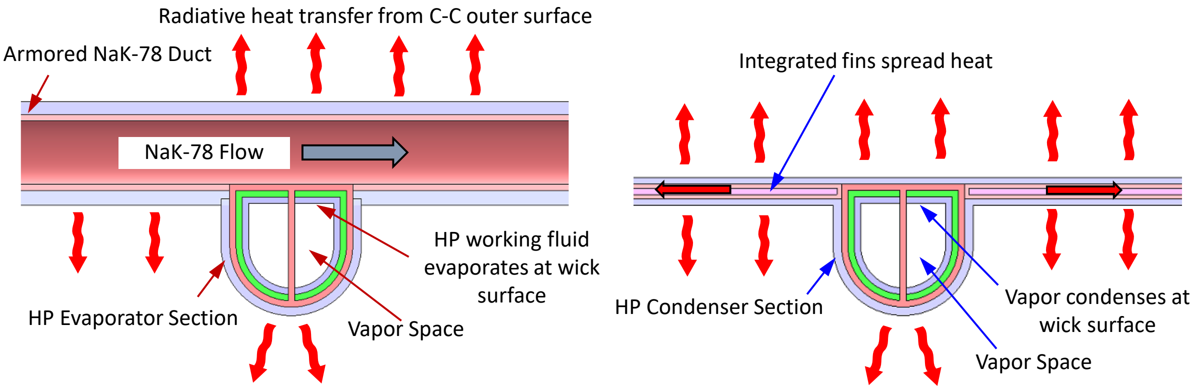

(b) Side view through heat pipe evaporator and duct A-A

(b) Side view through heat pipe condenser B-B

Figure 5: Illustrations of the heat transport and rejection pathways for the developed heat pipe radiator module Version 1 design in Fig. 4.

Figure 5 shows illustrations of the flow of heat pipe working fluid liquid from the condenser sections to the evaporator and of the working fluid vapor from the evaporator to the condenser sections of the heat pipes in the radiator module design in Fig. 4a. The thermal energy transfer from the flowing liquid NaK-78 in the header duct is by convection to the Ti duct wall and conduction through different layers of the structure in the heat pipe evaporator (Figs. 4a, b). The titanium wall of the liquid NaK-78 header is brazed directly to the Ti heat pipe wall. The convection/conduction heat transfer to the Ti wall of the heat pipes and across the heat conduction in the liquid annulus and the liquid saturated porous wick of the heat pipe evaporates the working fluid from the porous wick surface into the vapor flow region along the evaporator section of the heat pipe. The vapor traverses the heat pipe to the condenser sections where it condenses onto the porous wick surface and the liquid condensate flowing through the annulus to the evaporator section. The heat pipe design has been shown to raises both the wicking and the entrainment limits [1].

Since no credit is taken for the liquid condensate flow in the porous wick, it is possible to use a wick with small pore sizes and volume porosity to increase the capillary pressure head for circulating the working fluid in the heat pipe, and hence the power throughput, as well as raise the heat pipe entrainment limit. The heat from the heat pipe working fluid condensate transfers to the outer surface of the C-C armor covering the heat pipe and the HOPG/Ti/C-C fins to be rejected by thermal radiation into space. In addition, waste heat is rejected directly by thermal radiation into space from the surface of the C-C armor of the liquid NaK-78 header duct (Figs. 3-5).

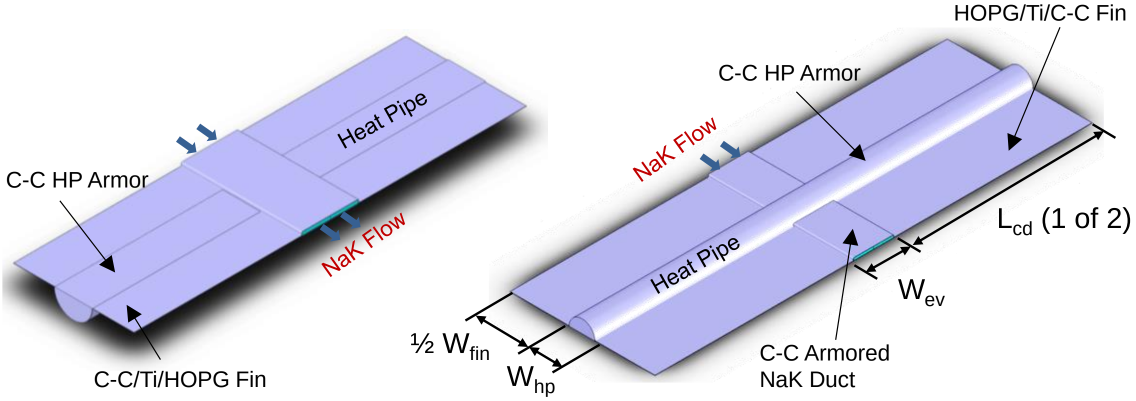

(a) Version 1 Heat Pipe Module/ver$_1$ **(b) Foldable Version 2 Heat Pipe Module/ver$_2$**

Figure 6: External views of the developed radiator module designs Version 1 and Version 2.

3.1.2. Developed Radiator Module Design Version 2

As illustrated in Figs. 4 and 5, the heat pipe radiator module design Version 1, or ver$_1$, has the heat pips laid along the outer surface of the panel (Figs. 3, 6a) on one side and the liquid NaK-78 duct laid across on the opposite side. The protruding duct and heat pipe on both sides of the panels may interfere with the compaction of the folded and stowed radiator panels during launch. To alleviate this issue, a foldable heat pipe radiator panel with another heat pipe module design Version 2 (or ver$_2$) is developed. It has a flat surface to enable more compact stowage of the heat rejection radiator array during launch.

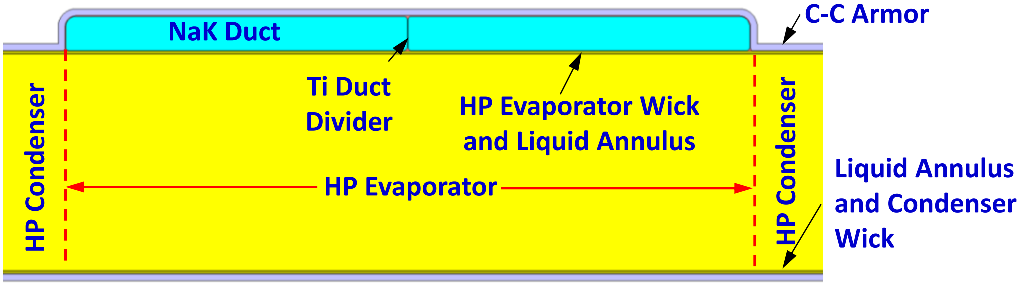

(a) Version 1 Heat Pipe Radiator Design

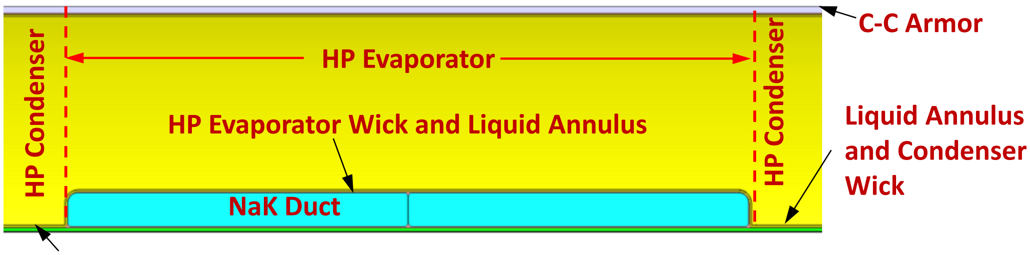

(b) Foldable Version 2 Heat Pipe Radiator Design

Figure 7: Sectional views of the developed heat pipe radiator module ver$_2$ design showing the liquid NaK-78 flow duct passing through heat pipe.

Figure 6b and Figure 7 present views of the foldable Version 2 of the radiator heat rejection module. In this design, the liquid NaK-78 flow placed above the plane of the HOPG/Ti/C-C heat spreading fins on the same side as the heat pipes (Fig. 8b). The heat spreading fin is extends along the entire surface of the radiator panel and in contact with the flat side of the heat pipe Ti wall. In contrast, the HOPG/Ti/C-C fin in the heat pipe radiator module design ver$_1$ only extends from the sides of the heat pipe condensers and NaK-78 flow duct (Fig. 8a).

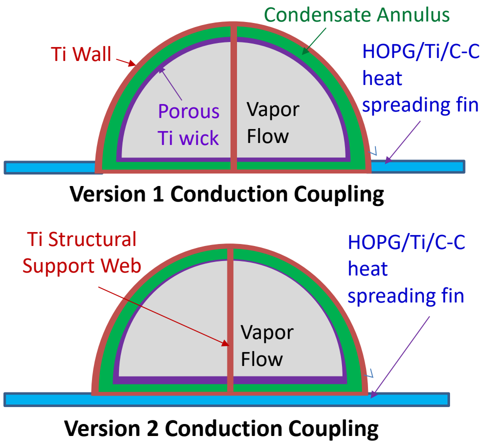

Figure 8: Sectional views of heat pipes contact with HOPG/Ti/C-C fins in modular ver$_1$ and ver$_2$ designs.

In ver$_2$ modular design, the NaK-78 duct passes through the heat pipe evaporator section with the Ti wall joined to that of the heat pipe evaporator (Fig. 7b). This design increases the evaporator surface area compared to the configuration in Version 1 (Fig. 7a). The liquid annulus and the Ti porous wick extend along the surface of the Ti wall to decrease the pressure losses of the liquid condensate return to evaporator. The continuous composite HOPG/Ti/C-C heat spreading fin also provides some protection to the Ti walls of the heat pipe and the NaK-78 duct. Furthermore, the total armor surface area is smaller than in the Version 1 design. The reduced amount of C-C armor in Version 2 design partially compensates for the increased mass of the fin covering the entire lower surface of the module (Figs. 8a, b).

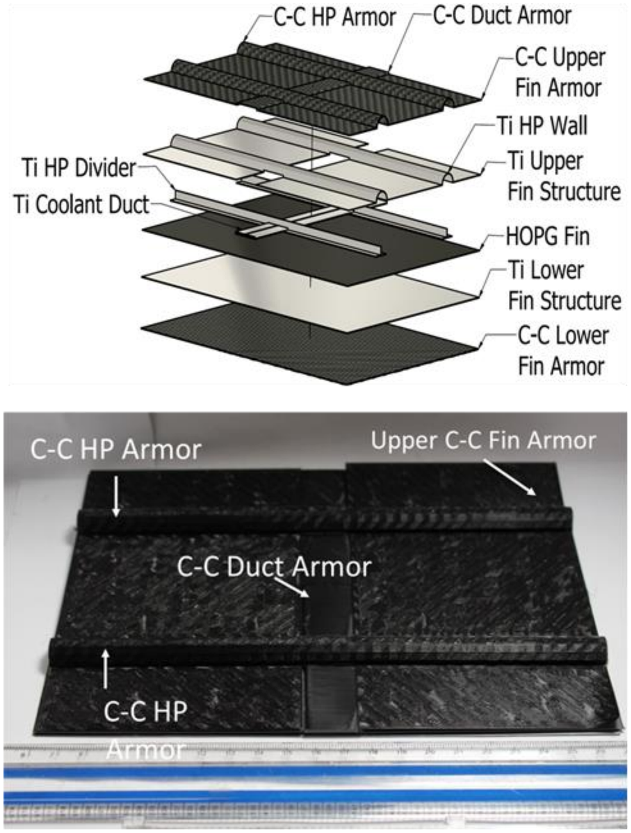

Figure 9: 3-D printed 1/10 scale of the heat pipe radiator module design Version 2.

3.2. Additive Manufacturing of Module Design Version 2

The project has developed a 3-D printing capability in the UNM-ISNPS lab to fabricate solid 3-D models of the developed heat pipe radiator module and components out of rigid plastic. The 3-D plastic modules are used for visualization during meetings and have assisted in further development of the design of the heat pipe radiator panel. Figure 9 shows an exploded CAD view of solid geometry and the assembled 3-D printed model of the Version 2 heat pipe radiator module with two heat pipes and associated heat spreading fins. It is planned to use this capability as the project advances to help explore the foldability of the modular heat pipe radiator panels for storage during launch before the panels are deployed once in orbit.

For the range of heat rejection surface temperatures of interest (500 – 600 K), the choice of the working fluid of the heat pipes impacts not only their dimensions and performance, but also those of the radiator modules and panels. For these temperatures, water is not a proper choice because of its high vapor pressure, and neither is potassium because of its low vapor pressure at the temperatures of interest. This research detailed in Section 4 below compares the choices of Cs and Rb alkali metal working fluids, with higher vapor pressures than potassium but lower than for water (Figure 9-11).

4. SELECTION OF HEAT PIPE WORKING FLUID

For temperatures ≤ 500 K, water is a suitable working fluid, but its high vapor pressure requires a thicker heat pipe wall. This combined with the low power throughput, increases the areal density of the radiator. The water heat pipe radiators are suitable for use in conjunction with dynamic energy conversion options, such as CBC turbomachinery and FPSE with low waste heat rejection temperatures. On the other hand, energy conversion technology options with waste heat rejection temperatures ≥ 600 K, radiator heat pipes could use alkali metals working fluids, with lower vapor pressure than water and the same or higher Figure-of-Merit (FOM).

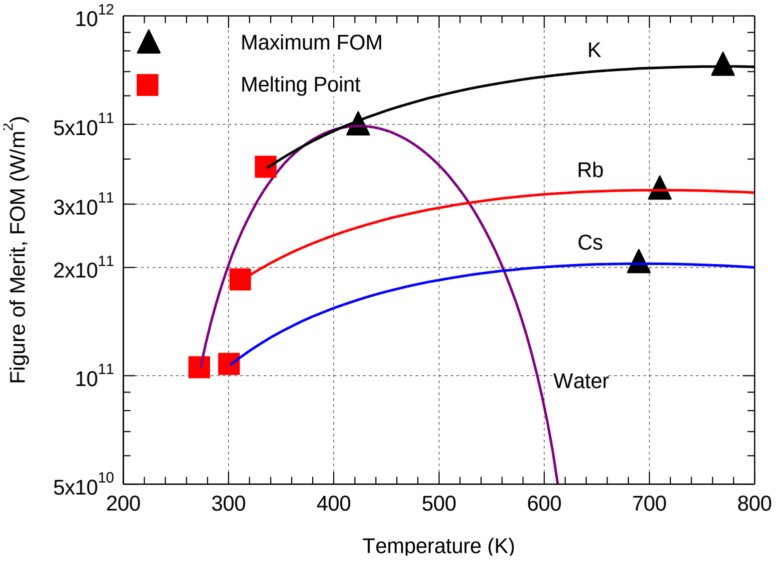

Figure 10: Figure of Merit (FOM) curves for Cesium, Rubidium, and Potassium heat pipe working fluids versus temperature.

Alkali liquid metal of Cs, Rb, K, Na, and Li working fluids operate at progressively elevated temperatures up to 1400 K and power throughputs to up to 30 kW/m^2 [9]. They are compatible with the lightweight titanium alloys that possess high melting temperature of 1,941 K and good thermal and physical properties over a wide range of operating temperatures [21]. A measure of the performance of the heat pipe working fluid is the figure of merit (FOM), defined as $\sigma_L \rho_L h_{fg}/\mu_L$, where σ_L is the liquid surface tension, ρ_L the liquid density, h_{fg} is the liquid latent heat of vaporization, and μ_L is the liquid viscosity (Fig. 10). All these properties are evaluated at the average evaporator temperature and corresponding vapor pressure in the heat pipe. For a given working fluid, best performance is at or near the temperature corresponding to the maximum FOM of the working fluid of choice (Fig. 10).

Unlike for water, the FOM curves for the alkali metals are flat near their maximum values. This allows using the alkali metal heat pipes over a wide range of temperatures near that at the maximum FOM, with slight decrease in performance and with thin wall because of their low vapor pressures (Fig. 11).

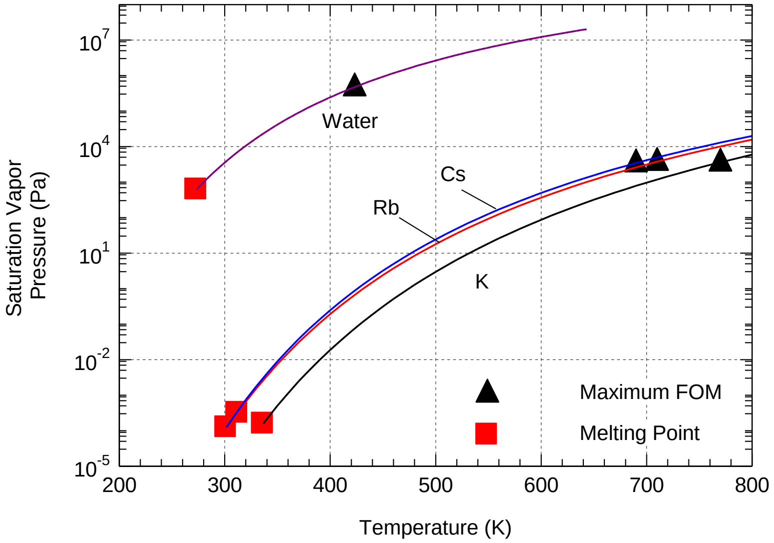

Figure 11: Comparison of saturation vapor pressures of heat pipe working fluids of interest

Nonetheless, FOMs for alkali liquid metals increases as their vapor pressures increase or the boiling temperatures decrease. For example, Cs and Rb fluids have lower vapor pressures than water, but higher than that for potassium (Fig. 11). Thus, for the 500 – 600 K temperatures of interest, Cs and Rb working fluids are suitable choices (Figs. 10, 11). At these temperatures, the potassium vapor flow in the heat pipes will not be in the continuum flow regime and the performance will be inferior to those of the Cs and Rb heat pipes. In the latter, vapor flow in the heat pipes will operate in the continuum flow regime and requires smaller heat pipe equivalent diameters (Fig. 11). As the target operating temperature range is comparatively low, Fig. 11 shows that cesium has the highest saturation vapor pressure that is slightly higher than for rubidium, while the potassium vapor pressure is significantly lower.

At 500 K and 600 K, the Cs vapor pressure increases by a factor of ~20, from 24.3 Pa to 495.4 Pa, respectively. The vapor pressure for water is significantly higher, ranging from 2.56 to 11.9 MPa. This high vapor pressure increases the required thickness of the heat pipe walls, the mass, and the axial heat conduction in the wall from the evaporator to the condenser sections of the heat pipes. Thus, water a poor choice for the heat pipe working fluid at the temperature range of interest (500 - 600 K).

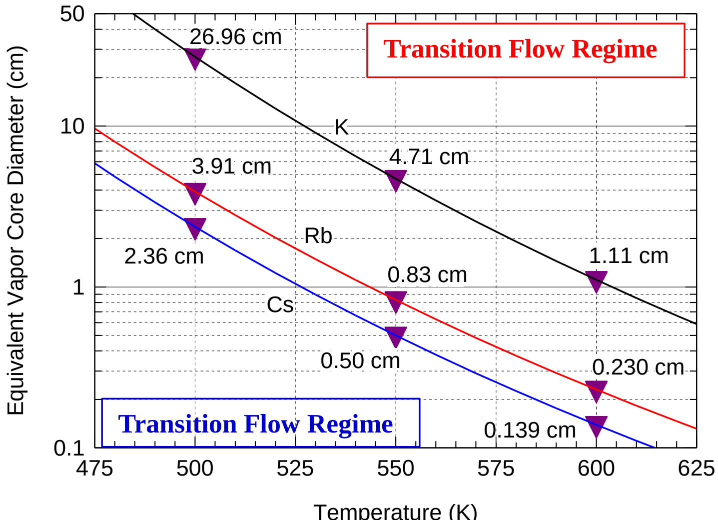

Figure 12: Het pipe equivalent diameters for operating in continuum and transition flow regimes of Cs, Rb, and K working fluids versus temperature

Furthermore, the vapor of the heat pipe working fluid needs to operate in the continuum flow regime. At lower temperatures and depending on the equivalent diameter of the vapor, the vapor flow would either be in the molecular or the transition flow regime, depending on the choice of the alkali metal working fluid (Figs. 11 and 12). The boundaries between the continuum and transition vapor flow regimes of Cs, Rb and K working fluids are compared in Fig. 12 [6, 21]. The plotted curves in this figure determine the smallest vapor flow equivalent diameters for Cs, Rb and K working fluids for operating in the continuum vapor flow regime versus the average heat pipe temperature.

Figure 11 shows the values of the smallest diameters for a potassium heat pipe to operate in the continuum flow regime of vapor at 500 K is 26.96 cm. This diameter decreases exponentially with increased temperature to 1.11 cm at 600 K. This excludes consideration of potassium as a heat pipe working fluid for the present application. The other two alkali metals of Cs and Rb, with lower FOMs as heat pipe working fluids but high saturation vapor pressures, have equivalent vapor flow diameters to operate in the continuum flow regime (Fig. 11) significantly smaller than for potassium. For a Rb heat pipe at 500 K, the smallest vapor equivalent diameter to operate in continuum flow regime is 3.91 cm, and decreases exponential to 0.83 cm at 550 K. For operating at 500 K the smallest equivalent diameter for continuum flow of the Cs working fluid is 2.36 cm, decreasing exponentially to 0.139 cm with increased temperature to 600 K. The smaller vapor diameters for operating the Cs vapor in the continuum flow regime are favored for achieving lower mass and areal density of the radiator module with HOPG/Ti/C-C heat spreading fins for rejecting waste heat rejection into space at 600 K.

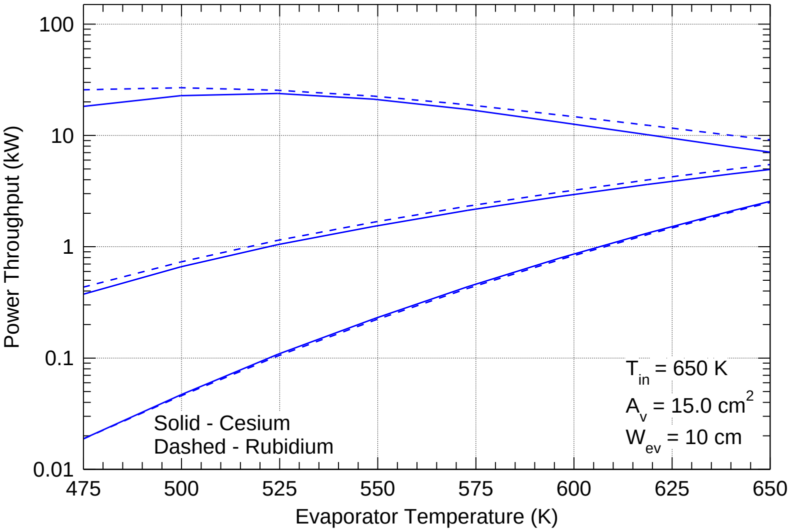

Figure 13: Comparison of operating limits of the heat pipe design in ver$_2$ module design with Cs and Rb working fluids versus evaporator temperature for 650 K inlet temperature of NaK-78 in header duct of the radiator module

In addition to determining heat pipe diameter to operate in the continuum flow regime, the selecting of the working fluid, it is important to also determine the prevailing limit of operation the heat pipe at the temperatures range of interest. The calculated heat pipe operating limits with Cs and Rb working fluids are compared in Fig. 13 versus the average heat pipe evaporator temperature. These are: (a) the capillary limit, Q_{cap}, which depends on the selected average pore size in the porous wick; (b) the entrainment limit, Q_{ent}, of the liquid from the porous wick by the counter current vapor flow, which depends on the properties of the vapor and liquid phases and surface tension of the working fluid, and the size of pores in the porous wick; and (c) the sonic limit, Q_s, which depends on the cross section area for vapor flow exiting the evaporator section of the heat pipe and the working fluid vapor pressure or density. The wicking limit depends on the flow pressure losses of the returning liquid condensate from the condenser to evaporator section of the heat pipe. This limit is raised using an annulus for the liquid condensate flow to the evaporator section in the current heat pipe designs.

At evaporator temperature, the highest power transport by the heat pipe at a given operating temperature is that corresponding to lowest or prevailing operation limit. For enhanced reliability and redundancy and avoidance of single point failures in the heat pipe radiator panels, the actual power transport is selected to correspond to 75% of the prevailing operation limit.

Figure 13 compares the sonic, entrainment, and capillary limits of the Rb and Cs working fluids at same vapor cross section flow area of 15.0 cm^2 (or equivalent vapor flow diameter = 4.37 cm) versus the evaporator temperature from 475 K to 650 K. The sonic limit, Q_s, is reached when the vapor exiting the evaporator section reaches the speed of sound, and the flow becomes sonically choked. This limit is low because of the low densities of the Cs and Rb vapors exiting the evaporator. The sonic limit is calculated at the vapor saturation temperature, $T_{ev,0}$, at that stagnation pressure at the end of the evaporator section of the heat pipe, $P_{ev,0}$ as [22]:

$$Q_s = 0.474\, A_v h_{fg}\left(T_{ev,0}\right) P_{ev,0} \sqrt{\frac{MW}{R_g T_{ev,0}}} \qquad (1)$$

In this empirical expression, A_v is the vapor flow area, h_{fg} and MW are the working fluid latent heat of vaporization and molecular weight, respectively, and R_g is the gas constant.

The entrainment limit, Q_{ent}, occurs when the sheer force imposed by the vapor flow at the surface of the liquid saturated porous wick exceed that of the liquid surface tension. The entrained droplets by the vapor flow return to the condenser, reducing the net liquid condensate flow to the evaporator section and risk causing a dry out at the inner surface of the heat pipe evaporator wall. The entrainment limit can be increased by reducing the pore radius in the wick, at the expense of decreasing the capillary pressure for driving the working fluid flow in the heat pipe, and hence the power throughput, or by increasing the equivalent diameter of the vapor flow in the heat pipe. This limit is calculated using the following expression [22], as:

$$Q_{ent} = h_{fg}\left(T_{ev,0}\right) \left(A_v \sqrt{\frac{MW}{R_g\, R_p}}\right) \sqrt{\frac{{P_{ev,0}}^2\, \sigma_l\left(T_{cd,0}\right)}{P_{cd,0}\, T_{cd,0}}} \qquad (2)$$

In this expression, $T_{cd,0}$ is the temperature at the stagnation pressure at the end of the condenser section of the heat pipe, $P_{cd,0}$, R_p is the radius of the pores in the sintered metal wick, and σ_l is the liquid surface tension at the operating temperature of the heat pipe.

The capillary limit, Q_{cap}, is determined from the momentum balance for the heat pipe working fluid where the capillary pressure generated at the end of the evaporator section minus that lost by condensation of the working fluid at the end of the condenser, ΔP_{cap}, equals the sum of the friction pressure losses for the vapor flow and the returning liquid condensate flow through the annulus, ΔP_l and ΔP_v, respectively. This limit can be expressed as [6]:

$$Q_{cap} = \frac{1}{\frac{4}{h_{fg} A_{an} {t_{an}}^2}\left[\frac{\mu_l\left(T_{cd,0}\right) L_{cd}}{\rho_l\left(T_{cd,0}\right)} + \frac{\mu_l\left(T_{ev,0}\right) W_{ev}}{\rho_l\left(T_{ev,0}\right)}\right] + \frac{dP_v}{Q}} \times \frac{2\, \sigma_l\left(T_{cd,0}\right)}{R_p} \qquad (3)$$

In this equation, A_{an} and t_{an} are the flow area and width of the liquid annulus, and L_{cd} and W_{ev} are the condenser and evaporator lengths, R_p is the geometrical radius of the pores in the porous wick, μ_l and ρ_l are the liquid viscosity and density at the evaporator and condenser saturation temperatures $T_{ev,0}$ and $T_{cd,0}$, respectively, and Q is the thermal power transported.

Figure 13 shows that the sonic limit is the prevailing operating limit for the radiator Rb and Cs heat pipes in the temperature range of interest in the present work (500 - 600 K). This is due to the low vapor pressures of these working fluids at these temperatures (Fig. 11). For the same heat pipe vapor flow diameter, the sonic limit of the Cs working fluid is slightly higher than that for the Rb working fluid. At the same temperatures, the entrainment, and the capillary limits for both Rb and Cs working fluids are markedly higher than the sonic limit. Based on these results, Cs is selected as the heat pipe working fluid in the developed designs of the heat rejection radiator modules. The higher Cs vapor pressure decreases the heat pipe diameter for operating the vapor in the continuum flow regime and increases the sonic limit for operation at target temperatures.

4. MOST SIGNIFICANT TECHNICAL ACHIEVEMENT(S)

The most significant technical achievements among those detailed in the next section include the development and investigation of the preliminary performance of two designs of lightweight heat pipe radiator modules (ver$_1$ and ver$_2$) in Figures 4 - 7. The emphases have been on an average surface temperature of 600 K for radiative rejection of waste heat into space and liquid NaK-78 inlet temperatures in the header duct of the radiator module of 625 and 650 K. Similar work is done for lower 500 K surface temperature, which showed large increase in the areal density of the radiator and decease in the sonic limit of the heat pipe.

- Using a HOPG layer, encased in Ti in the heat spreading fins has been shown to be effective in spreading the heat, decreasing the areal density, and increasing the power density of the radiator panel. Adding HOPG fillets have shown to enhance the thermal conduction coupling of the heat pipes to the HOPG/Ti/C-C heat spreading fins by decreasing both the thickness of the HOPG layer in the fins. They also help enhance the structural rigidity of the radiator panels but may slightly increase the areal density of the radiator model.
- For operating at average surface temperatures for heat rejection of 500 – 600 K, Cs and Rb heat pipe working fluids are being shown to be the only viable choices. However, Cs is preferable based on the lower temperature and equivalent heat pipe diameter needed to operate in the continuum flow regime and the lower vapor pressure to use a thinner Ti heat pipe wall, and hence decreasing the areal density of the radiator.
- The operation of the developed heat pipe designs with Cs and Rb working fluids is sonic limited because of their low vaper densities at the temperature of interest. Nonetheless, heat pipe power throughput for the Cs working fluid is higher for increased heat pipe evaporator temperature and inlet temperature of liquid NaK-78 in the radiator header duct. This liquid adds to the areal density of the radiator while the exposed surface area of the duct contributes to the total heat rejection by the heat pipe radiator into space and hence, decreasing its areal density.
- Results suggest that achieving an areal density of 4 kg/m^2 is possible with the developed advanced radiator panel concepts at average surface temperature of 600 K, subject to future improvements to attempt approaching or reaching the NASA stated target of ≤ 3 kg/m^2. For a lower surface average temperature of 500 K for waste heat rejection into space, the power density of the radiator is significantly lower, and the areal density is higher than at 600 K. However, at both temperatures, the estimates of the radiator areal densities are markedly lower than current SOA.
- Performed 3-D CFD analyses of a heat pipe radiator module effectively identified needed improvements to enhance the thermal conduction coupling of the Cs heat pipes to the HOPG/Ti/C-C heat spreading fins. The addition of HOPG fillets helps decease the thickness of the HOPG layer in the heat spreading fins and the overall areal density of the heat pipe radiator module.
- To ensure strong diffusion bonding at the interfaces of the Ti casing in the heat spreading fins with both the HOPG and the C-C composite armor, magnetron sputtering of Ti on graphite and C-C specimens has been effective in producing continuous 1-2 μm thick Ti layers. Preliminary characterization the Ti interfacial layer deposited on C-C composite samples using SEM microscopy techniques is very promising.

In summary, the two design concepts of lightweight heat rejection radiators are promising for achieving areal densities significant lower that the current SOA, but still short of the NASA desired target of ≤ 3 kg/m^2. The Cs heat pipe working fluid in the modules of the radiator panel is suitable for operating at the indicated heat rejection surface temperatures of 500 – 600 K. The developed heat pipe designs raise the entrainment and the wicking limits, but their operation at the temperatures of interest is the sonic limited because of the low vapor pressure of Cs. The current TRL of the developed radiator design concepts and investigated during the first 11 month of the

ESI award is 3.0 – 4.0 and could be higher subject to demonstrating fabricability of the developed designs of the lightweight Cs heat pipe radiators with HOPG/Ti/C-C heat spreading fins.

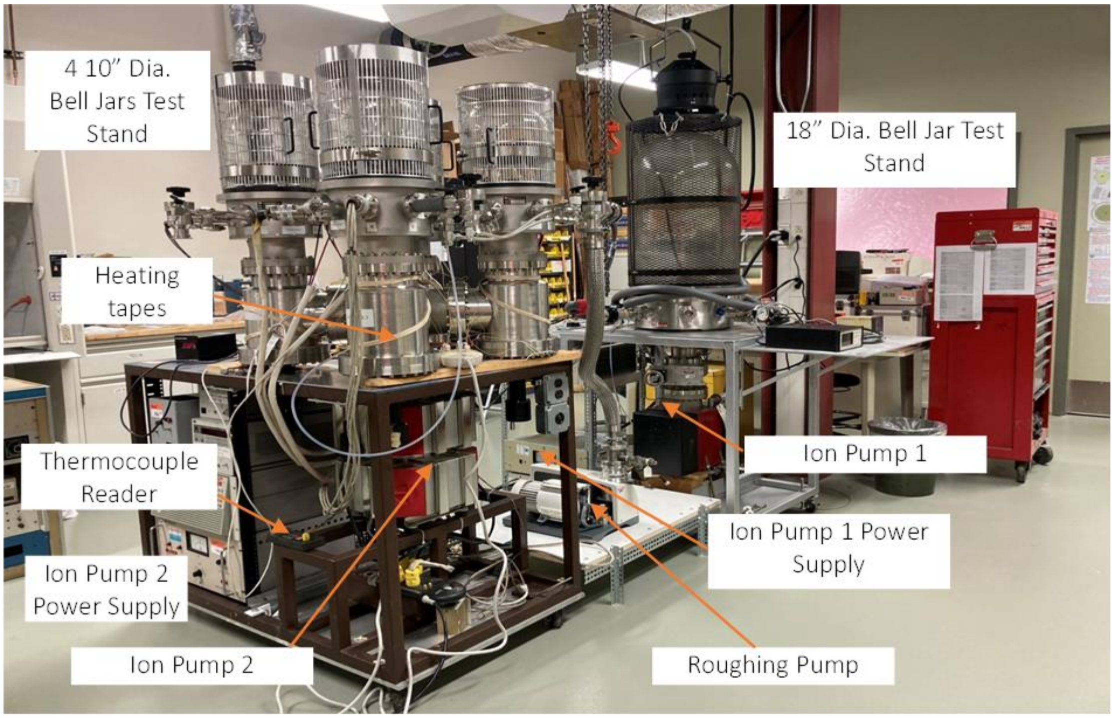

Figure 14: UNM-ISNPS vacuum facility with 4-10" bell jar and 18" bell jar test stands.

5. ACTIVITIES AND ACCOMPLISHMENTS

This section lists the accomplishments made in less than 11 months of the first year of the NASA ESI award as contrasted to the stated objectives in the award proposal documents. During the above performance period, our research team at the University of New Mexico Institute for Space and Nuclear Power Studies (UNM-ISNPS) and the Nuclear Engineering Department are as follows:

- Performed analysis and selected the appropriate heat pipe working fluid for operating at an average heat rejection temperature of 500 K - 600 K. Results show that at these temperatures Cesium (Cs) is a better choice than Rubidium (Rb) and the heat pipe operation will be sonic limited because of low vapor densities of these working fluids. The higher vapor pressure of Cs increases the sonic limit and hence the power throughput. The performed analysis also determined the heat pipe diameters to ascertain that at the above temperatures the Cs vapor in the heat pipes is in the continuum flow regime.
- Developed an integrated lumped parameter model of heat pipe radiator modules of distinctive designs using the capabilities of the MATLAB Simulink framework [23]. Each is comprised of a Cs heat pipe thermally coupled to an integrated HOPG/Ti/C-C composite heat spreading fin with C-C composite armor, and a liquid NaK-78 header flow duct thermally coupled to the evaporator section of the heat pipe. Performed analyses using the developed lumped model investigated the effects on heat pipe power throughput, and the areal density, dimensions, and specific power of the radiator module of the following parameters, namely: (a) the of width and length of the heat spreading HOPG/Ti/C-C fins (the length of the fins equals that of the condenser of the Cs heat pipes in the modular); the equivalent heat pipe diameter or the flow area of the Cs vapor in the heat pipes; (c) the inlet temperature of the NaK-78 in the header duct, and (d) the average surface temperature for heat rejection.

- Incorporated a heat pipe physics-based model into the Star-CCM+ commercial CFD code [24] to model of the vapor flow within the heat pipes with vapor injections from the porous wick along the evaporator length and vapor condensation along the length of the condenser. This model will also estimate the curvatures of the menisci of the liquid vapor interface in the heat pipe porous wick at the ends of the evaporator and condenser sections of the heat pipe, and solve the coupled continuity, momentum and energy balance equations for the heat pipe working fluids as functions of the temperature of the NaK-78 flow in the header duct of the radiator module and the module dimensions and design.
- Investigated methods of enhancing thermal coupling of the heat pipes to the heat spreading HOPG/Ti/C-C fins armored with C-C composite for achieving an average heat rejection temperature of 600 K. These include varying the thickness of the HOPG layer in the heat spreading fins and using HOPG fillets with different curvatures between the heat pipe Ti wall and the HOPG/Ti/C-C heat spreading fins. The effectiveness of these methods is quantified using 3-D CFD-thermal analyses of the heat pipe radiator module. These analyses the employed the Star-CCM+ commercial code [24] calculated the heat flow field and the spatial distribution of the surface temperature for NaK-78 temperatures of 650 K and 625 K in the flow duct of the heat pipe radiator module.
- Investigated the performance of two advanced heat pipe radiator panel designs for performance and foldability. Performed analyses compared the effects of the design and dimensions of the heat pipe radiator module on the areal density as functions of the radius of curvature and angle of the thermal coupling fillets between the Cs heat pipes and HOPG/Ti/C-C fins, the thickness of the HOPG layer in the heat spreading fins, and the inlet temperature of the NaK-78 liquid in the header duct of the module.
- Prepared samples of C-C composite and graphite for the deposition of Ti then layer (1-2 mm thick) on the surface for subsequent characterization of the diffusion bonding at the interfaces. Samples of C-C composite, isotropic pyrolytic graphite and HOPG are prepared using magnetron sputtering at the Department of Energy's Center for Innovative Nanotechnologies (DOE-CINT) Gateway users' facility at Los Alamos National Laboratory (LANL). The cost is underwritten by DOE for the users of the CINT facility based on the approval of the users' submitted proposals. The prepared Ti and graphite samples are ground and polished to a smooth surface to enhance the diffusion bonding of the Ti deposited using magnetron sputtering. To date, performed Ti deposition on the C-C and graphite samples at the LANL CINT facility is at room temperature and at 500 °C. Received samples are characterized using optical microscopy and Scanning Electron Microscopy (SEM) to determine the quality and approximate thickness of the deposited Ti layers. The optical and SEM analysis characterizing the interface between the C-C substrate and the deposited Ti layer is performed using the existing SEM facility at UNM. Future examination and characterization on the diffusion bonded interfaces with different substrates of C-C and HOPG can also be performed in the CINT user facility.
- The coated C-C composite and graphite samples to date at LANL are prepared and mounted for imaging using the optical and SEM imaging. They show continuous ~1.4 – 2 μm thick Ti coating of the carbon fibers in C-C composite samples and on the polished graphite surfaces. Characterization of the Ti – C-C and Ti-Graphite interfaces is being conducted using SEM microscopy techniques to examine and characterize the interfaces.
- Updated the vacuum facility at the UNM-ISNPS in preparation for the planned outgassing of the HOPG and C-C specimens coated with Ti in hard vacuum of ~1-4 x10^{-7} torr for subsequent investigation of the effect on the quality of the diffusion bonding at the interfaces. The UNM vacuum facility comprises four 10" diameter bell jar test stand and 18" bell jar test stand which are operational and have been evaluated for continuous operation at 2-4x10^{-7} torr (Fig. 14)
- Established an additive manufacturing 3-D printing facility at the UNM-ISNPS and utilized it to produce 3-D models of the heat pipe radiator module designs and components out of rigid

plastic for visualization and improving the developed designs of the liquid-weight advanced radiator panel concepts.

6. UNM-ISNPS VACUUM FACILITIES

The UNM-ISNPS Vacuum Test Facilities (Fig. 14) have been refurbished and are currently operational in preparation for outgassing the specimens of HOPG and C-C coated with magnetron sputtered Ti at the DOE CINT user facility. One test stand has an 18" diameter bell jar and the second test stand has 4-10" diameter bell jars each with an isolation vacuum valve. Both facilities share a roughing pump to reach 10^{-4} torr, but each has separate ion pump for hard vacuum of 1-5 x 10^{-7} torr (Fig. 14). The facility is ready for vacuum testing of Ti coated HOPG and C-C composite samples to evaluate how any outgassing due to exposure to hard vacuum will affect the materials interfaces and its properties.

7. DEVELOPED HEAT PIPE RADIATOR MODEL

A heat pipe lumped model is developed to perform parametric analyses to investigate the effects of design options of the performance, dimensions, and areal density of the two developed designs of heat pipe radiator module with Cs heat pipes. A radiator module comprises a single Ti - Cs heat pipe that is conductively coupled to the heat spreading HOPG/Ti/C-C composite fins. The heat pipe evaporator section is thermally coupled to the liquid NaK-78 flowing in the header duct of the module. The developed heat pipe model assumes the evaporator is uniformly heated and the condenser section rejects waste heat radiatively into space. The heat rejection from the outer surface of the condenser and fins assumes a uniform outer surface temperature, T_s, and surface emissivity of 0.85. The model also accounts from the radiative heat rejection for the exposed surface of liquid NaK-78 heater duct and from the edges of the heat pipe and the HOPG/Ti/C-C composite heat spreading fins. The radiative waste heat rejection is to an environmental sink temperature of 250 K, which would represent those for a near-Earth or lunar surface environment.

The calculated radiative heat flux from the outer surface of the radiator module is used to determine the corresponding surface temperature of the porous sintered Ti wick inside the heat pipe along the length of the condenser sections using a thermal conduction resistance model. These temperatures are used to determine the liquid surface tension at the surface of the porous wick and together with the calculated vapor stagnation pressure determine the curvature of the liquid meniscus in the pores of the wick along the condenser and evaporator sections. The liquid surface tension and the geometrical radius of the pores in the porous wick, taken equal to 25 μm, are used to calculate the maximum capillary pressure possible for circulating the Cs working fluid in the heat pipe and compare it the calculated evaporator and condenser capillary pressures.

The calculated total flow rate of vapor, based on the thermal power input to the evaporator section and the latent heat of vaporization of the Cs working fluid at the liquid temperature in the porous wick at the end of the evaporator, is used in the momentum balance equation of the working fluid in the heat pipe. This equation equates the net capillary pressure generated in the heat pipe to the sum of the calculated pressure losses for the vapor flow through the central region of the heat pipe and for the liquid condensate flow in the 0.25 mm wide annulus between the porous wick and the inner surface of the heat pipe Ti wall (Figs. 3 and 4). This liquid annulus reduces the liquid pressure losses and raises the capillary limit of the heat pipe (Fig. 13). The calculated capillary pressure in the evaporator is added to the saturation vapor pressure at the temperature of the liquid-vapor interface to determine the stagnation pressure at the end of the evaporator (located at the symmetry plane).

The present heat pipe model account for axial conduction in the 0.2 mm thick Ti wall of the between the evaporator to the condenser sections and accounts for the changes in the properties of the solid structure materials, Cs liquid and vapor, and liquid NaK-78 with temperature. The calculated total friction pressure losses for the vapor flow and the liquid condensate flow in the annulus account for vapor injection at the surface of the porous wick in the evaporator section and condensation analog the condenser [25]. The pressure loses for the liquid Cs condensate in the annulus are determined using a friction factor relationship for liquid in an annulus covered by a porous wick [26].

7.1. Lumped heat pipe model results

The developed lumped heat pipe model is used to investigate the effect of the liquid NaK-78 inlet temperature to the header duct on the radiator module and the width of the HOPG/Ti/C-C composite fins, W_{fin}, on the performance and masses of the Version 1 and Version 2 module designs. The parametric analysis is for the heat pipes operating at 75% of the prevailing sonic limit. This allows for up to 25% redundancy in the operation of the heat pipes radiator panel. The external outer diameter of the half-circular heat pipes, D_c, is kept constant at 6.5 cm. The HOPG/Ti/C-C fins are joined to the heat pipe without a HOPG fillet, and with the HOPG layer in the fins is 0.45 mm thick. The width of the heat pipe evaporator, W_{ev}, is kept at 10 cm while the length of the heat pipe condenser sections, L_{cd}, is varies with the heat transfer surface area required to radiatively reject the heat transported by the heat pipe from the flow NaK-78 liquid in the header duct. From the calculated dimensions of the heat pipe radiator module, the lumped parameter model calculates the mass and areal density.

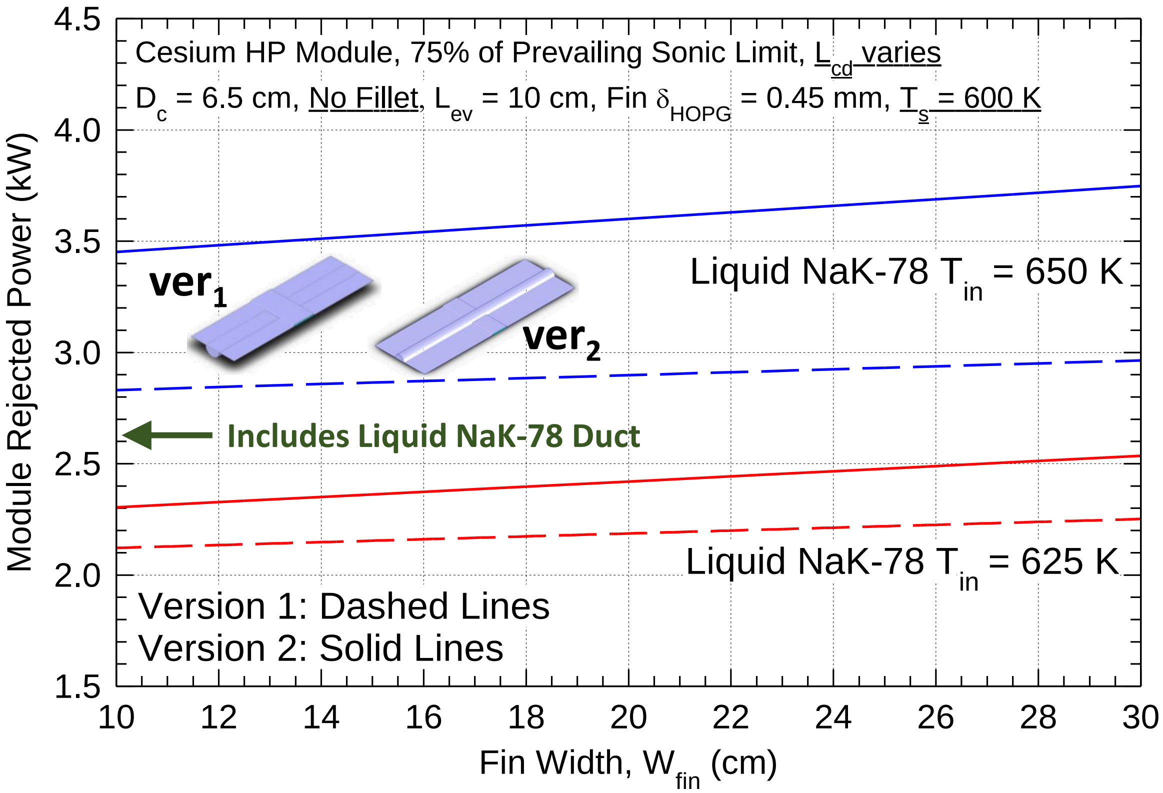

Figure 15: Comparison of rejected power by Version 1 and Version 2 designs of the heat pipe radiator module.

Figure 15 compares the calculated values of the rate of heat rejection for the heat pipe radiator modules into space for the Version 1 and 2 designs of the radiator module. The total rate of heat rejection includes those of the heat transported by the heat pipe and rejected from the surfaces of the condenser and heat spreading HOPG/C-C/Ti fins as well as that radiated directly from the surface of the NaK-78 duct. The rate of heat rejection increases with increased fin width, W_{fin}, due to the increased heat rejection surface area for the duct. The length of the flow duct for the module is equal to the sum of the fin width, W_{fin}, and the heat pipe curvature diameter, D_c. The long duct increases the heat rejection area with increased width of the fins. The rejected thermal powers from the Version 2 heat pipe radiator design are higher than for Version 1 design, because of the larger surface area for the former (Fig. 15).

The higher heat rejection area increases the evaporator temperature and hence, the operating sonic limit for the heat pipe (Fig. 13). The difference in the heat rejection between Version 1 and Version 2 designs increase with increased liquid NaK inlet temperature, T_{in}, from 650 K to 625 K. The lower 625 K NaK inlet temperature decreases the evaporator temperature, which decreases the power throughput for the Cs heat pipes. This decreases the total rate of heat rejection for the heat pipe radiator module into space (Fig. 15). The Version 2 heat pipe module with NaK-78 T_{in} = 650 K could reject from 3.45-3.75 kW_{th}, compared to 2.83-2.96 kW_{th} for Version 1 for the same T_{in}, representing an increase of 22-26%.

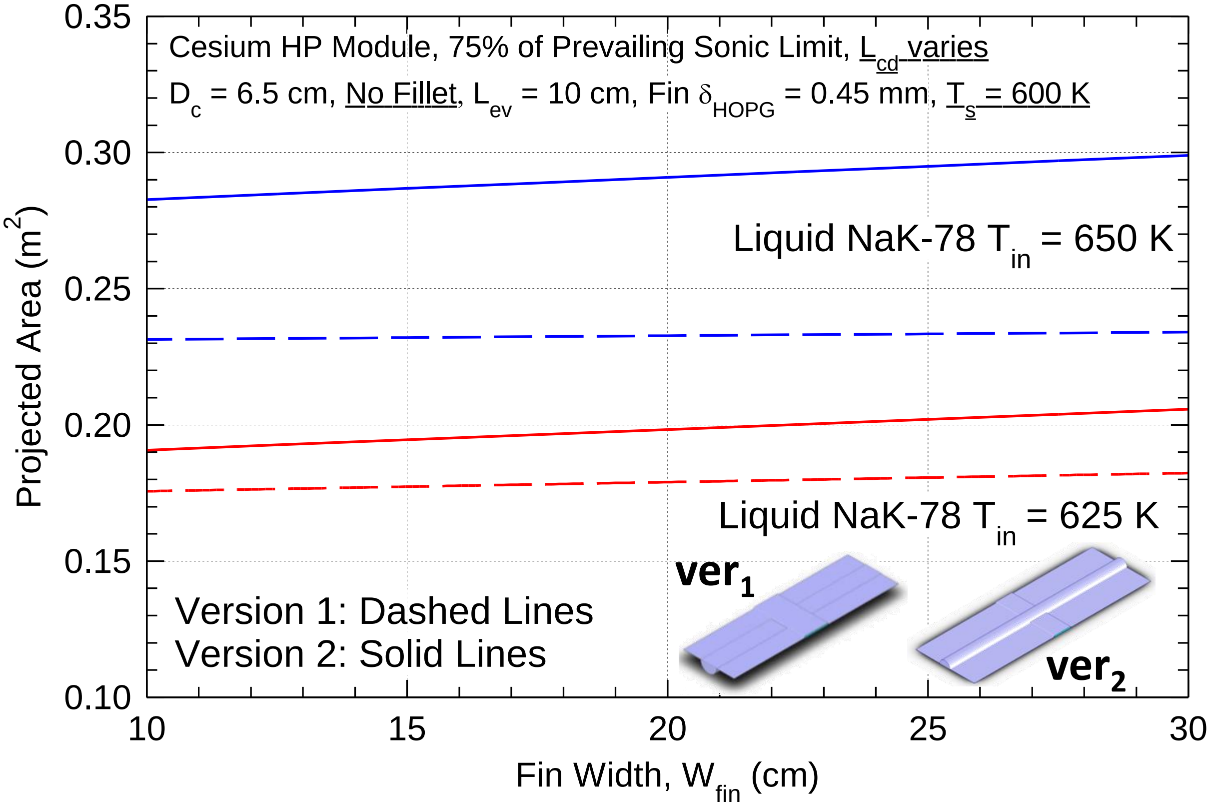

Figure 16: Projected area for radiative rate of heat rejections of Version 1 and Version 2 designs of the radiator module at surface average temperature, T_s = 600 K.

The calculated total projected areas in Fig. 16 include those of the flow duct, the heat pipe, and the HOPG/Ti/C-C fins. The results presented in this figure show that the radiator module heat rejection area increase slightly with increased width of the heat spreading fin, and more with increased inlet temperature of the flowing liquid NaK-78 in the header duct of the modules. As the width of the heat spreading fins increases the length of the heat pipe condenser decreases to achieve the necessary area to reject the transported heat into space (Fig. 17). The heat pipes for the Version 2 module design are up to 171.4 cm long for the shortest fin width of 10 cm, and decrease gradually to 81.9 cm for the widest fin width of 30 cm. The higher power throughput of the Cs heat pipes in the Version 2 module design requires longer heat pipes for the same fin width, or wider fins for the same heat pipe length. Similarly, the lower heat rejection at the lower liquid NaK-78 inlet temperature of 625 K requires shorter heat pipe length for a given W_{fin}.

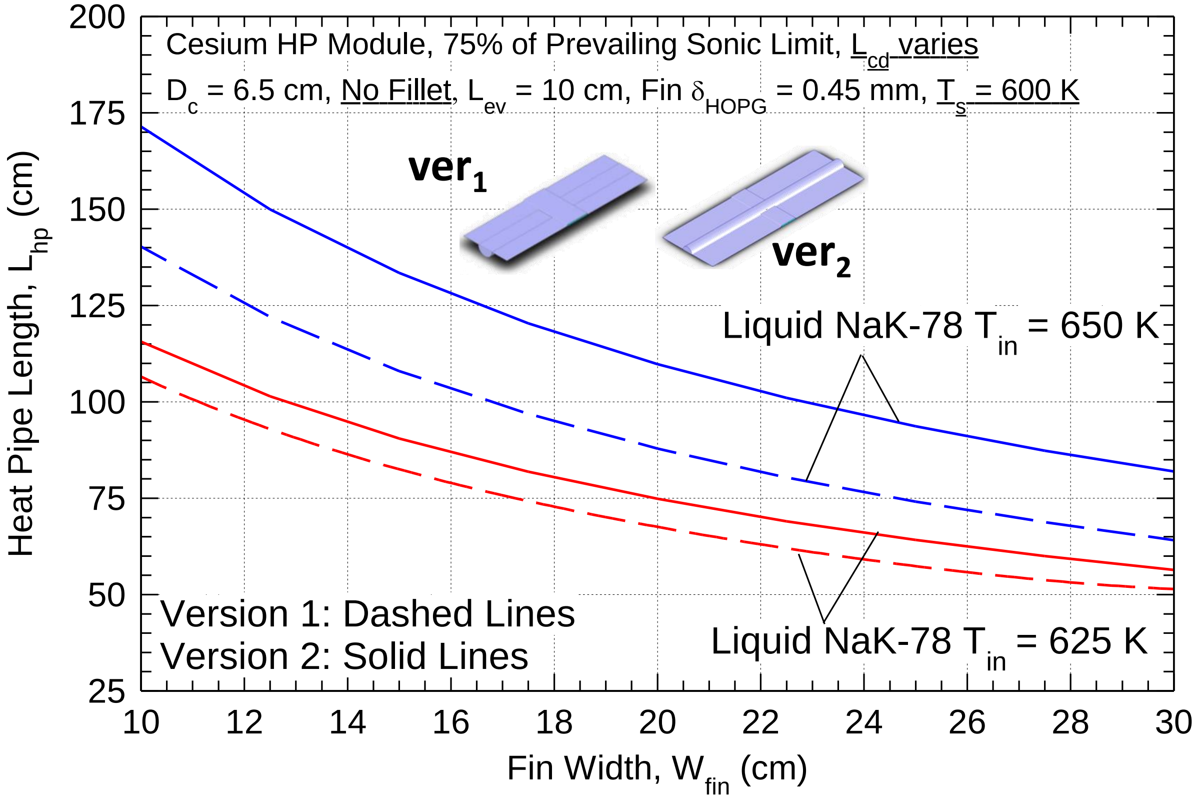

Figure 17: Comparison of the calculated total length of Cs heat pipes in Version 1 and Version 2 radiator module designs for water heat rejection at surface average temperature T_s = 600 K.

Figure 18 compares the calculated areal densities of the developed designs of the heat pipe radiator modules. The masses of the Cs heat pipe, HOPG/Ti/C-C heat spreading fin, and NaK-78 flow duct are calculated using the density values and red bolded thicknesses listed in Table 2. For a given projected area, the heat spreading fins contribute the lowest fraction of the total mass of the module. For the higher liquid NaK-78 inlet temperature of 650 K, the areal density of the Version 2 heat pipe radiator module design decreases from 4.4 kg/m^2 with a fin width of 10 cm to 3.6 kg/m^2 with the wider fin of 30 cm (Fig. 18). The corresponding areal densities for the Version 1 module design with NaK-78 T_{in} = 650 K are 12-13% higher than those for the Version 2 design and range from 4.9 - 4.1 kg/m^2.

The results of the parametric analysis using the lumped parameter model indicate that the Version 2 heat pipe radiator module design increases the rate of heat rejection and decreases the areal density. The results also show that a fin width of 30 cm results in a lower areal density of the heat pipe module. Based on these results Version 2 module design is selected for further analysis. The obtained performance results using the lumped heat pipe model are for surface average temperature, T_s = 600 K and HOPG layer thickness, δ_{HOPG} = 0.45 mm. In the following subsection the performed 3-D CFD thermal analyses investigate the effect of increasing the thickness of HOPG fillets (Fig. 19) on improving the heat transfer from the heat pipe to the heat spreading fins for achieving T_s = 600 K. The analyses also investigate the effects of the HOPG fillets on the variation in the surface temperature of the heat spreading fin.

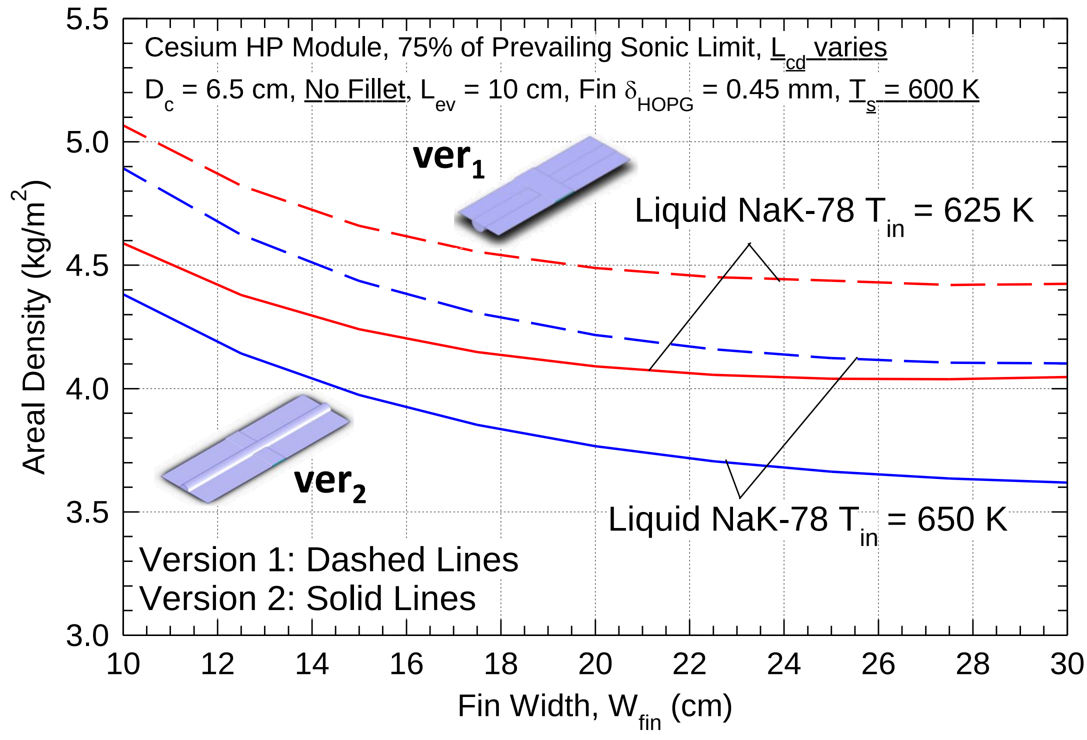

Figure 18: Comparison of areal densities of Version 1 and Version 2 heat pipe radiator modules with HOPG/Ti/C-C fin at surface average temperature, T_s = 600 K.

7.2. 3-D CFD Heat Transfer Analyses of Heat Pipe Radiator Module

The conducted 3-D, CFD thermal analyses of a Version 2 heat pipe module using the commercial Multiphysics code Star-CCM+ [24] investigate the thermal coupling of the Cs heat pipe to the heat spreading HOPG/Ti/C-C composite fins. The analysis also investigates the effects of using HOPG fillets of different curvatures, or angle θ, to enhance thermal coupling of heat pipe to the heat spreading fins, on the spatial distributions of surface temperature and the heat flux for heat rejection into space. Figure 19 illustrates the structure of the HOPG fillets for thermally and structural coupling the Cs heat pipe to the heat spreading HOPG/Ti/C-C composite fins. Increasing the angle of the fillet, θ, increases the contact area for heat conduction from the heat pipe Ti wall to the heat spreading fins, and thus expected to enhance the uniformity of the surface temperature of fins and the total rejection of waste heat into space. The performed 3-D, CFD thermal analysis determines the HOPG layer thickness and fillets' angle to achieve an average heat rejection surface temperature of 600 K.

The commercial Multiphysics code Star-CCM+ [24], used to investigate the performance of a single heat pipe module, employed polyhedral mesh cells and imbedded thin meshes to generate the volume mesh cells in the thin structural members in the heat pipe module that include the Ti wall, the liquid Cs annulus, and the porous wick. The generated mesh elements for performing the calculation ranged

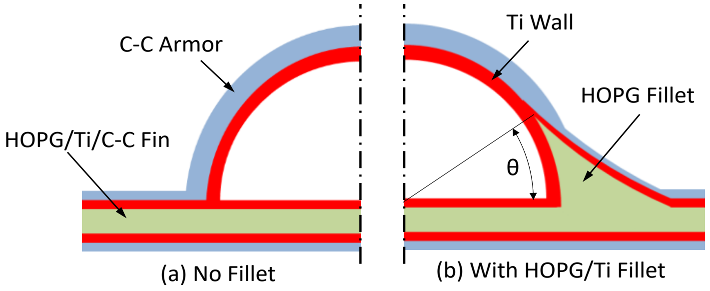

(a) No Fillet
(b) With HOPG/Ti Fillet

Figure 19: HOPG fillets for enhanced conduction coupling of heat pipe to HOPG/Ti/C-C fins.

from 0.05 to 1.5 mm is size and totaled 28.39 million cells. A cross section view of the used meshing is shown in Figure 20. Two layers of prismatic mesh cells are used in the thin solid regions of the heat pipe radiator structure, with 0.36 million cells in the HOPG, 1.09 million cells in the C-C armor, and 6.14 million cells in the Ti wall. The Cs vapor region in the heat pipe employs prismatic mesh cells and 5 prism layers with 0.5 mm total thickness at the interfaces, for a total of 19.13 million cells.

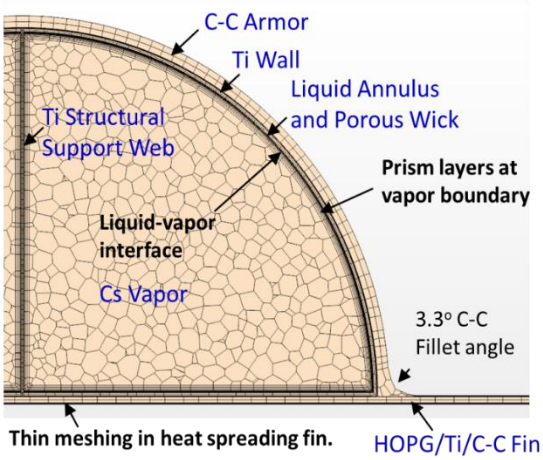

Figure 20: Numerical meshing in CFD simulations of Version 2 radiator module.

The CFD calculations account for the temperature dependent properties of the solid material and liquid Cs and vapor in a single heat pipe heat rejection module. The cesium vapor is simulated as an ideal gas using the compressible gas model in Star-CCM+. The liquid cesium flow in the heat pipe annulus is not modeled at this time, but the heat conduction through liquid Cs is considered. The interfacial thermal resistances between the different material layers in the module are neglected. The 3-D, CFD numerical model of a single heat pipe radiator module calculates the rate of heat transfer by convection and conduction from the liquid NaK-78 flow in the header duct to the heat pipe evaporator. The rate of heat transfer from the liquid NaK-78 in the header duct to the heat pipe evaporator surface determines the generation and injection rate of the Cs vapor into the heat pipe flow region from the surface of the porous wick. Heat transfer from the NaK-78 liquid duct inner surface to the C-C armor and the HOPG/Ti/C-C composite fins is eventually rejected by radiation into space.

The surface temperature in the condenser is calculated from linearly interpolating the vapor stagnation pressure between the ends of the evaporator and condensers. The Star-CCM+ code calculates the surface heat flux based on the calculated surface temperature. The total heat flow rate at the evaporator wick inner surface is compared to that determined at the surface of the wick in the condenser of the heat pipe to ensure overall heat balance. In addition, the CFD model of the heat pipe radiator module calculates for the friction pressure losses for the vapor flow and in the liquid flow annulus along the length of the heat pipe. The vapor injection and condensation rate in the evaporator and condenser sections, respectively, occur within 0.05 mm wide nuclear grid cells along the inner surface of the porous wick in the heat pipe. The outer surfaces of the C-C composite armor, the heat spreading composite fins, and the liquid NaK-78 header duct in the numerical analysis are subject to an environmental radiation boundary condition to a sink temperature of 250 K. The grey-thermal radiation model calculates the view factor for each surface numerical cell using ray tracing. An external emissivity value of 0.85 is used for the outer surfaces of the radiator panel in the simulations

7.3. *3-D, CFD thermal analysis results*

The commercial CFD code Star-CCM+ is used to perform 3-D thermal analyses of Version 2 heat pipe radiator module design to investigate the effectiveness of the thermal coupling between the Cs heat pipes and the HOPG/Ti/C-C fins using HOPG fillets. These analyses investigate the case with no HOPG fillets and with HOPG fillets angles, q, of 15° and 30° (Fig. 19) to enhance the thermal coupling between the heat pipes and fins. The Star-CCM+ results are for heat pipe evaporator width, W_{ev} = 10 cm, heat pipe length, L_{hp} = 110 cm, and HOPG/Ti/C-C composite fin width, W_{fin} = 30 cm. The simulations vary the thickness of the HOPG in the fins from 0.35 to 1.0 mm and investigated the effects of increasing the liquid NaK-78 inlet temperature in the header duct ,T_{in}, from 625 K and 650 K, on spatial temperature distribution for waste heat rejection to space.

Figure 21 presents images of the calculated temperature fields at the upper surfaces of the heat pipe radiator module for achieving cases of average surface temperature, T_s, of ~600 K. Results are for T_{in} = 650 K without with the 30° HOPG fillets. The fillets reduce the temperature difference, ΔT, across the surface from 111 K with no fillets and d_{HOPG} = 0.5 mm to 109 K with 30° fillets and δ_{HOPG} = 0.35 mm. The fillets angle enhances the heat spreading and decrease the surface temperature, ΔT.

Figure 22a compares the values of ΔT on the surface of the heat pipe radiator modules for T_s = 600 K, with increased fillets' angle and/or the thickness of the HOPG layer, δ_{HOPG}, in the heat spreading fins. For T_{in} = 650 K the δ_{HOPG} decreases from 0.45 mm without fillet to 0.35 mm with 30° HOPG fillets.

For liquid NaK-78 T_{in} = 625 K, achieving T_s = 600 K, require smaller fillets angle but thicker δ_{HOPG}. With no fillet, the δ_{HOPG} in the heat spreading fins = 0.78 mm and decreases to 0.5 mm with 30° fillets. The smaller ΔT with HOPG fillets could decrease the induced thermal stresses in radiator module but increases its total mass and areal density (Fig. 22b).

Despite the thicker HOPG in the heat spreading fins with no fillet, the areal density of the rejection radiator module is always the lowest, for T_{in} value of 625 and 650 K. For the heat pipe radiator module with 15° fillets, the mass of the fillets is slightly greater than the mass savings due to the thinner HOPG layer in the heat spreading fins, causing a slight increase in the areal density (Fig. 22b). As the angle of the fillets increases to 30°, their mass exceeds the savings of using thinner HOPG layer in the heat spreading composite fins and increases the areal density of the radiator module.

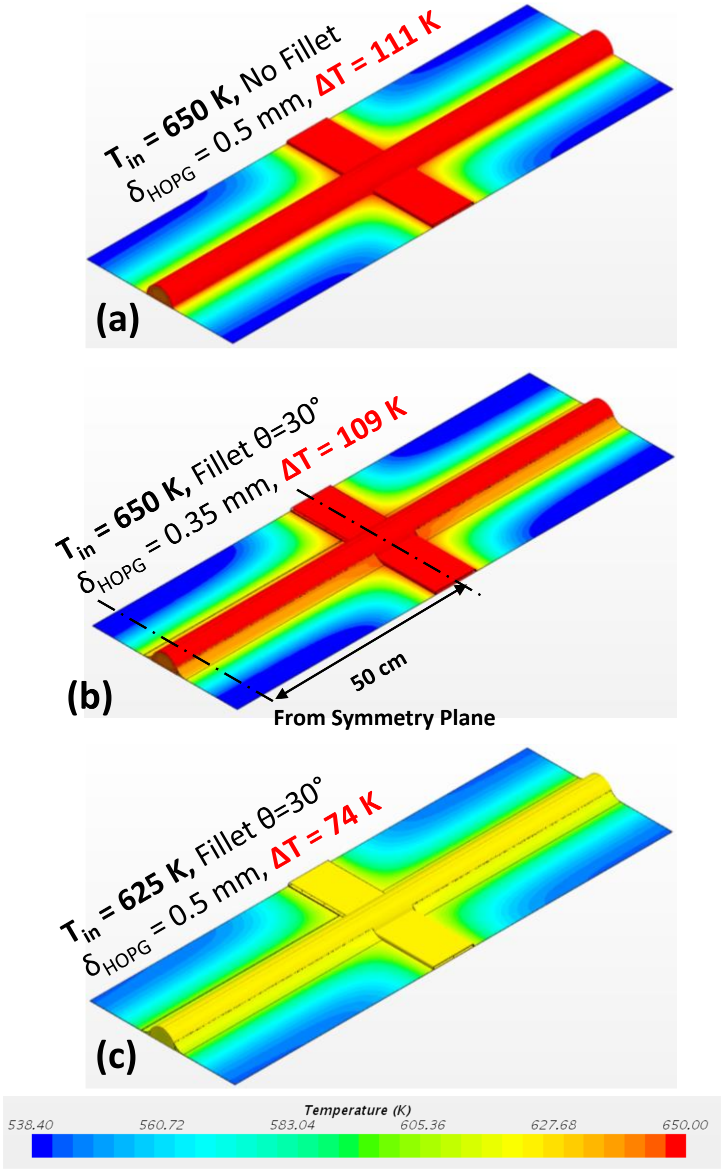

Figure 21: Local surface temperatures for Version 2 radiator module without and with 30° HOPG fillets.

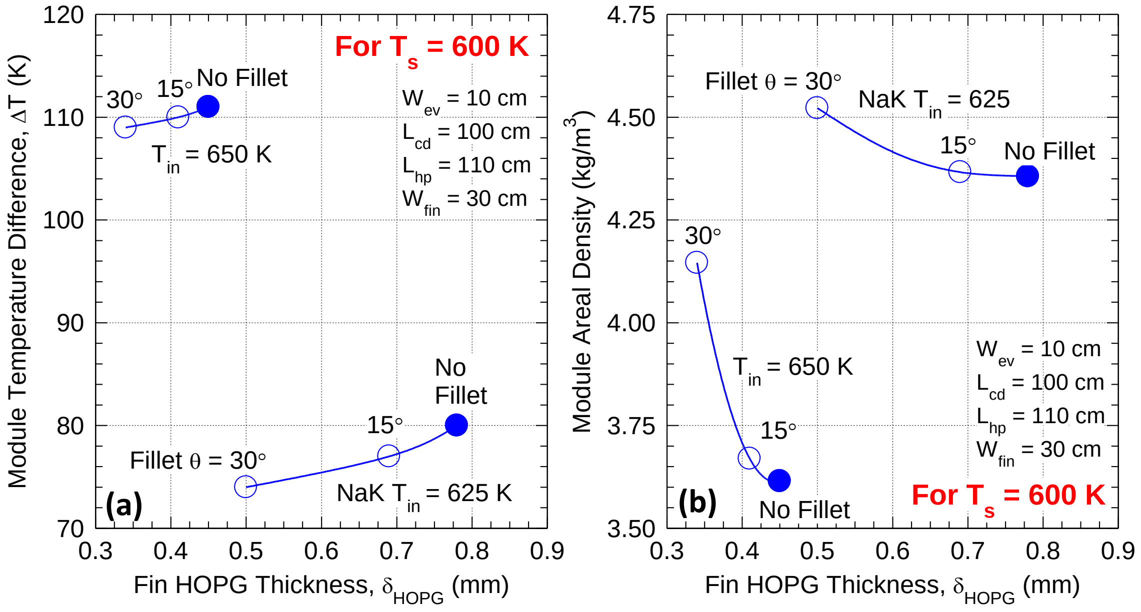

Figure 22: Effect of Fillets angle and δ_{HOPG} in heat spreading fins on difference in surface temperature, ΔT, and areal density of Version 2 radiator module design for achieving average surface temperature T_s = 600 K.

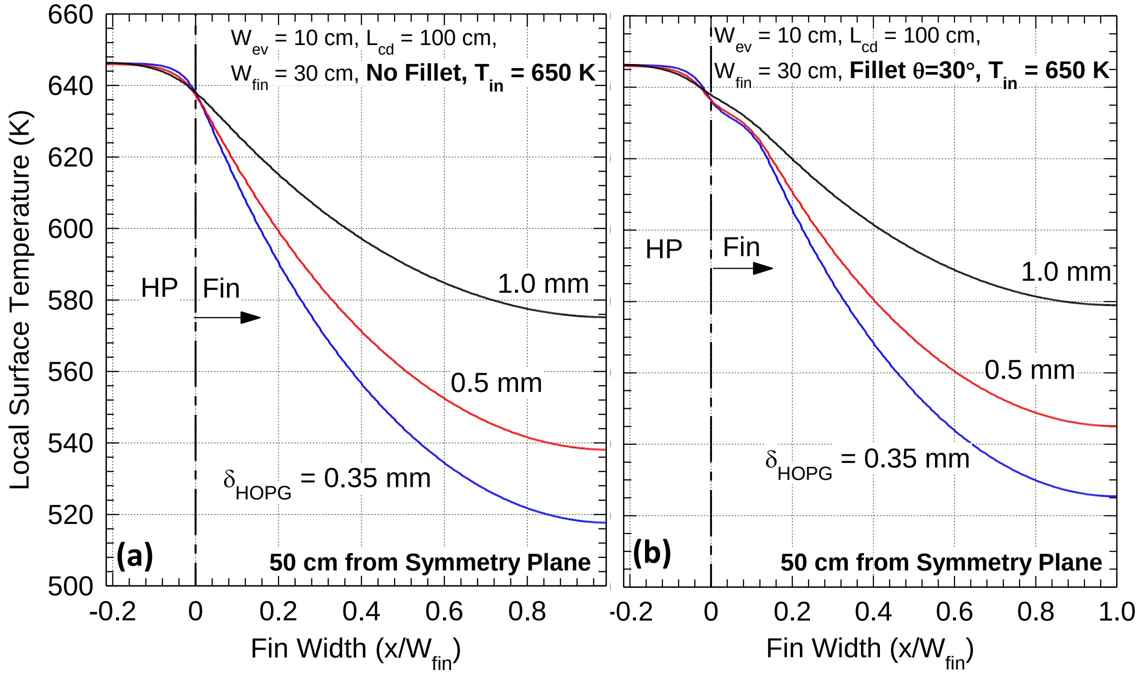

Figure 23: Local surface temperature profiles 50 cm from symmetry plane in the heat pipe radiator modules with: (a) no fillets and (b) 30° fillets, and for T_{in} = 650 K.

Figures 23-25 plot the calculated local surface temperatures across the surface of the heat pipe radiator module, 50 cm from the symmetry plane (at the location indicated in Fig. 21b). Figures 23a, 23b compare the local temperature profile the module surface temperature without and with 30° fillets for NaK-78 T_{in} = 650 K. Increasing the thickness of the HOPG in the heat spreading fins decreases the temperature drop along the fins. The effect of the HOPG fillet on the surface DT is more pronounced with the thinner δ_{HOPG} values of 0.35 and 0.5 mm than with the 1.0 mm thick HOPG layer (Figs. 23a and b). The increase in the local surface temperature along the fin with fillets is shown clearly in Figures 24a and b for heat pipe modules with T_{in} = 650 K and 625 K and δ_{HOPG} = 0.5.

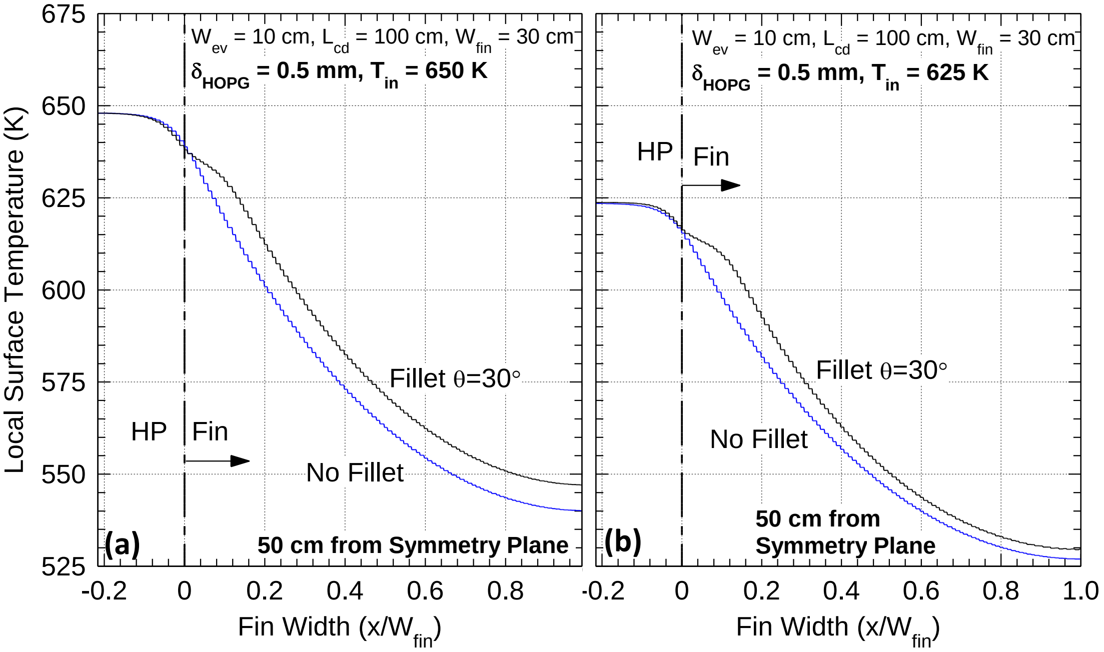

Figure 24: Local surface temperature profiles, 50 cm from module symmetry plane, for heat pipe radiator modules with δ_{HOPG} = 0.5 and (a) T_{in} = 650 K (b) T_{in} = 625 K.

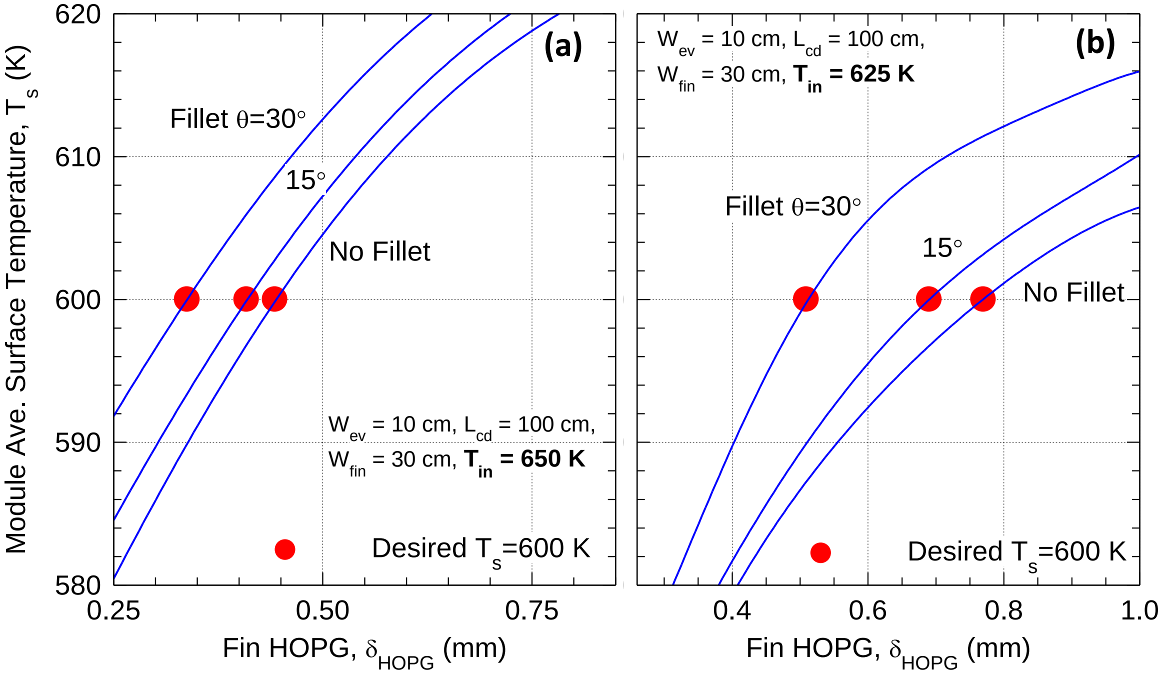

Figure 25: Module average surface temperature T_s with increasing δ_{HOPG} in heat spreading fins of heat pipe radiator modules with (a) T_{in} = 650 K and (b) T_{in} = 625 K.

The surface temperature profiles without and with 30° HOPG fillets are the same along the width of the Cs heat pipe. The high lateral thermal conductivity of the HOPG reduces the temperature drops near the root the heat spreading fins (Fig. 24). This enhances heat spreading and decreases the temperature differential across the fin for achieving the average surface temperature for heat rejection, T_s = 600 K. Figure 25 shows the change in the module average surface temperature T_s with increasing the HOPG thickness in the heat spreading fins. For T_{in} = 650 K the HOPG thickness to reach the desired T_s = 600 K, decreases from 0.45 mm without fillets to 0.41 mm, and 0.35 mm with 15° and 30° fillets, respectively. At the lower T_{in} = 625 K, the corresponding values of δ_{HOPG} in the heat spreading fins 0.78 mm, 0.69 mm, and 0.50 mm, respectively.

The results of the 3-D CFD thermal analyses show that for a HOPG/Ti/C-C fin width of 30 cm the desired average surface temperature for heat rejection of T_s = 600 K is achieved for the Version 2 heat pipe radiator module deign without fillets and with δ_{HOPG} = 0.45 mm. The corresponding areal density of the module is the lowest. The calculated areal density for this heat pipe radiator module of 3.62 kg/m^2 is lower than those for SOA heat pipe radiator concepts (Fig. 2) but is higher than the goal of ≤ 3 kg/m^2. Results also show that using HOPG fillets reduce the temperature difference along the surface of the radiator module, potentially reducing thermal stresses, but at the cost of increased areal density (Fig. 22).

8. INVESTIGATION OF DIFFUSING BONDING AT INTERFACES

This subsection presents the results of investigating diffusion bonding at the interfaces between Ti and both graphite and CC composite for prepared specimens. Magnetron sputtering is used to apply thin Ti layers onto the surfaces of the C-C composite and graphite specimens. This Ti deposition is performed in the DOE's CINT users' facility at LANL free of charge to the project. Preliminary characterizations using optical microscopy and Scanning Electron Microscopy (SEM) imagery are conducted to examine the deposited Ti layer and diffusion bonding to C-C composite and graphite. Demonstrating strong and reliable joins of Ti / C-C composite and Ti / HOPG via diffusion bonding at the interfaces is a key to the fabrication of the developed lightweight heat rejection radiator concept.

Prior work joining C-C composites with Ti used either elevated temperature adhesives or interfacial brazes. Cerny and Morscher [13] have investigated joining C-C composites to commercially pure Ti using elevated temperature adhesives. Samples were evaluated at temperatures from 600 K to 770 K. Tests at 600 K showed degradation, suggesting 530 K as an operating limit. Stanzi and Jaworske [27] and Jaworske, Stanzi, and Siamidis [28] have investigated joining Ti walled water heat pipes to graphite foam saddles using different elevated temperature adhesives. Both showed adequate joining for water heat pipe radiators rejecting heat at ≤ 500 K. Lan et al. [14] have investigated joining together C-C composites using a Ti_3SiC_2/SiC interfacial layer. Testing showed that a reliable joining was achieved, with the formation of TiC at the interface.

Moutis et al. [29] have experimented with joining C-C composites with Nimonic alloy using a TiCuSil braze, showing that the Ti-rich infill resulted in a strong interfacial bond with the C-C substrate. Morscher, et al. [12] investigated brazing Ti tubes to C-C composite plates with TiCuNi, TiCuSil, and Cu-ABA braze materials. Fracture testing demonstrated a strong bond, with testing showing failure occurring within the C-C composite layers rather than at the location of the bond. While T- and Cu based brazes achieved the strongest joints, reported results [30] also suggested that pure titanium may work for direct diffusion bonding.

In the present work, deposition of thin titanium films on HOPG and C-C composite samples is performed using magnetron sputtering. 1-2 microns thick deposited Ti layers are deposited on surface prepared samples of C-C composite and polished, graphite, and HOPG. Optical microscopy and SEM techniques are used to characterize the morphology of the surfaces and interfaces with substrates. Transmission Electron Microscopy (TEM) will be performed to characterize the Ti/graphite and Ti/C-C composite interfaces at the atomic scale and determine the extent of C diffusion into the thin Ti layer in the 2nd and 3rd years of the project. Ti coated samples of C-C composite and HOPG will be exposed to hard vacuum of ~1-4x10^{-7} torr in the vacuum test facility at the UNM ISNPS to investigate the effect of outgassing on the integrity of the diffusion bonded interfaces.

The magnetron sputtering deposition is performed at the DOE CINT user facility by J. Kevin Baldwin of LANL for C-C composite and conventional graphite (Fig. 26). The prepared samples to be coated are loaded into the sample handling chamber where a conveyer takes them into the sputtering chamber. The titanium target is biased at a negative potential. The negative potential causes free electrons to accelerate away from the target and ionize the injected flow of argon (Ar) gas atoms. The positive Ar ions are then strongly attracted to the negatively charged titanium target. When the Ar ions strike the target, they sputter off Ti atoms from the surface which deposit onto the sample substrate within the chamber (Fig. 26b) [31].

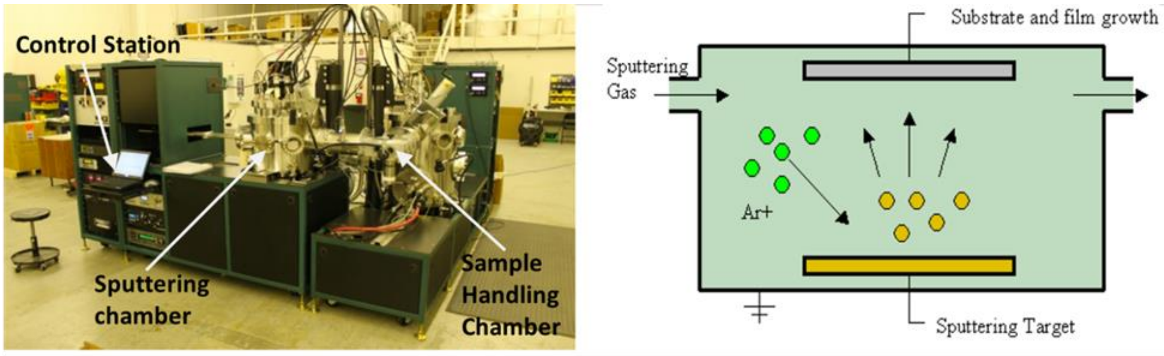

(a) Magnetron Sputtering Facility at CINT

(b) Magnetron Sputtering Process

Figure 26: Magnetron sputtering facility at the CINT Gateway facility at LANL [from 31].

The success of the diffusion bonding techniques is highly dependent on the surface finish of the sample materials. Considering this requirement, graphite sample surface preparation is completed using standard metallography techniques [32]. Prior to evaluating the HOPG, conventional pyrolytic, graphite is used for testing. Thin graphite samples are cut to size from a 2 cm diameter mandrel using a low-speed saw with a 4-inch diamond resin bonded wayfaring blade. To achieve a smooth surface, the surface of the specimens is prepared using plane grinding in steps, using 240-grit and up to 1200-grit sandpapers (Fig. 27a). The samples are sent to the CINT gateway facility where titanium is deposited at a power level of 300 Watts DC at a pressure of 3x10^{-3} torr Ar atmosphere. A 2-inch titanium target of 99.99% purity is used with a deposition rate of 0.2 nm/s. The sputtering deposition is performed at 500 °C to improve the adhesion to the graphite substrate. At this temperature, the stable titanium carbides should form in solution with Ti or C in the regions where diffusion occurs along the interface should form at the interface [33]. Figure 27b shows one of the polished graphite samples following the deposition of the Ti layer. Half of the samples are coated and mounted in epoxy resin for examination using optical microscopy and the other half are mounted for SEM analyses and characterization of the interfaces. The 2 cm diameter coated graphite disks are scored and split in two halves before being mounted in the resin for optical microscopy.

Commercial C-C composite 0.05” thick sheeting with CM-257-6 fibers is acquired from the Ceramaterials supply company. Preparing the carbon-carbon composite for joining is more challenging due to the presence of macro-level features (such as the ridges created by the intertwining fibers) at the surface of the composite. Strips of carbon-carbon composite sheet are removed from the feedstock using handheld shears. The strips are then cut to 1 cm x 1 cm squares using a low-speed saw. No grinding or polishing is performed of the surface of the C-C composite samples being coated with titanium via magnetron sputtering at the CINT facility.

Figure 28 shows images of several of the C-C composite samples before coating (Fig. 28a) and after the surface deposition of titanium (Fig. 28b). The woven fiber pattern in the C-C composite samples can clearly be seen in the images. The magnetron sputtering is performed with the samples heated to a temperature of 500°C. After coating, half of the samples are mounted in epoxy resin for optical microscopy and the other half are left saved for performing characterization of the interfaces using SEM analyses Techniques.

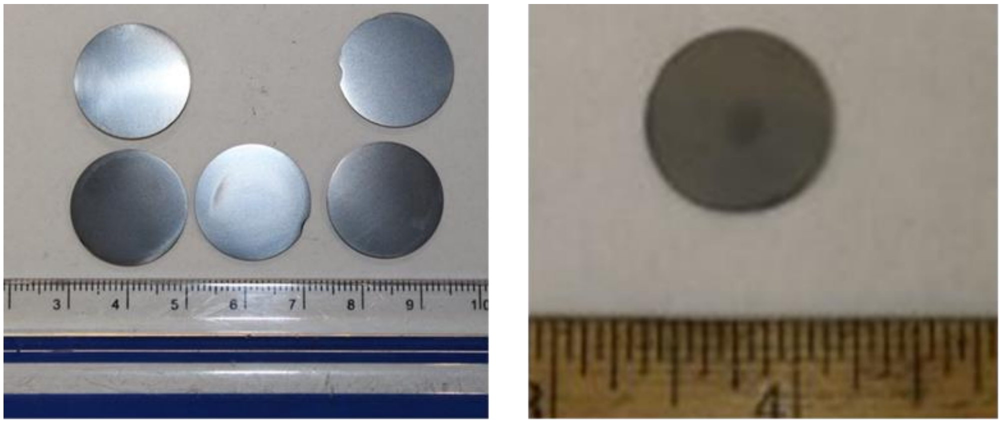

(a) Graphite samples before deposition

(b) Graphite disk following Ti deposition

Figure 27: Graphite samples (2 cm diameter tokens) used in magnetron sputtering experiment (a) before coating, and (b) following Ti layer deposition at 500 °C by magnetron sputtering.

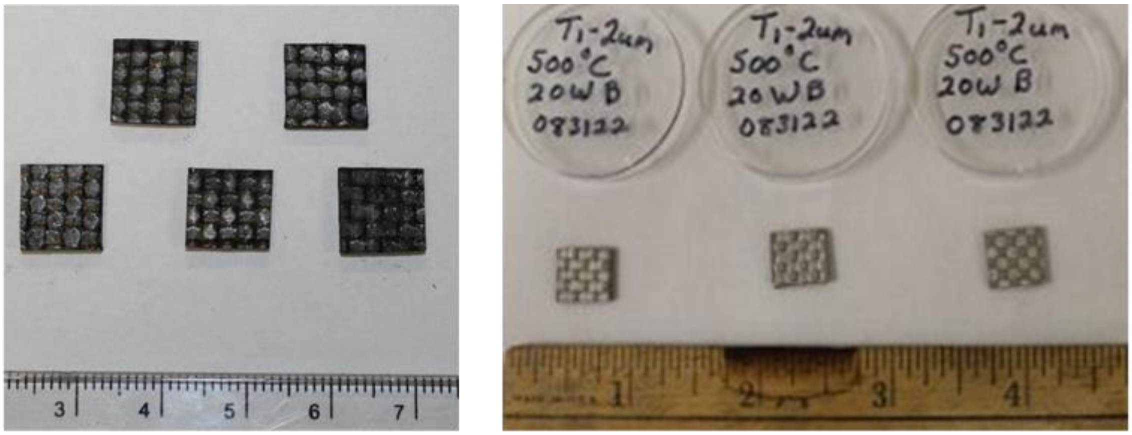

(a) C-C composite samples before coating

(b) C-C composite samples with titanium coating on upper surface

Figure 28: 1 cm x 1 cm samples of C-C composite samples before and after deposition of 2 µm thick Ti layer on upper surface.

Figure 29 shows images of the Ti coated specimens when examined using optical microcopy. The image of the mounted Ti-coated graphite sample shows a continuous, even layer of Ti deposited on the surface of the graphite (Fig. 29a). Optical microscopy of the coated C-C composite shows that the rough surface features results in an inconsistent deposition of the titanium layer (Fig. 29b). The imaged section of the coated C-C composite mounted sample is at a location where the strands of carbon fibers run parallel to the page, appearing as vertical light grey strands in Fig. 29b. The Ti layer is consistent for portions along the length of the carbon fibers, but the image also shows gaps in the coating. These gaps could be caused by shadowing effects where the rough surface morphology blocks the coverage from some of the Ti atoms sputtered from the target.

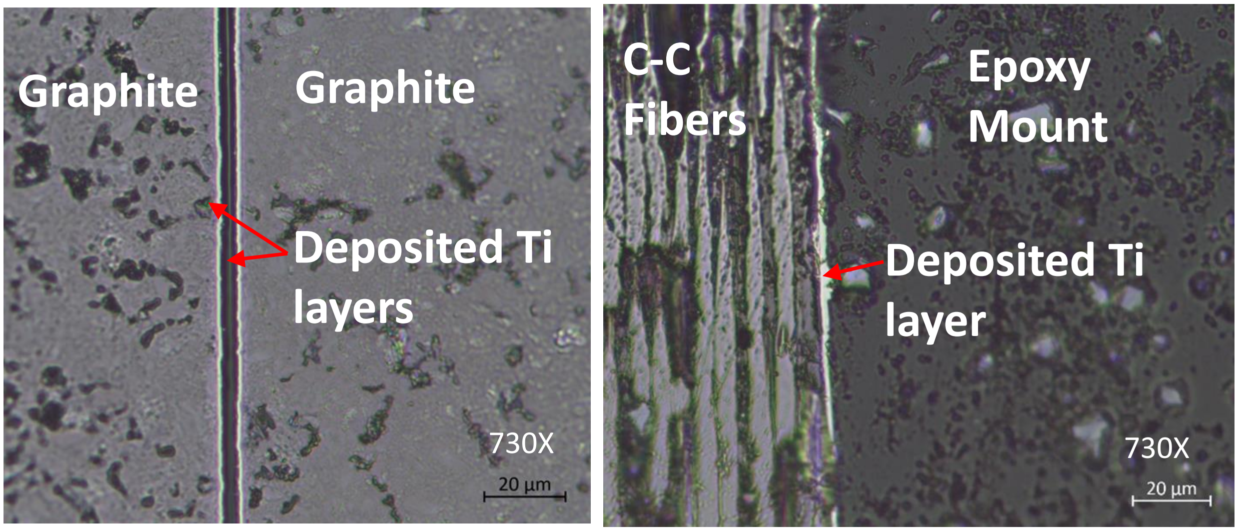

(a) Ti Coated Graphite

(b) Ti Coated C-C, showing in-plane fibers.

Figure 29. Cross section views of the graphite and C-C composite specimens with titanium coating. The image in (b) shows the two halves of the graphite sample facing each other following scoring and splitting with the coated surfaces facing each other.

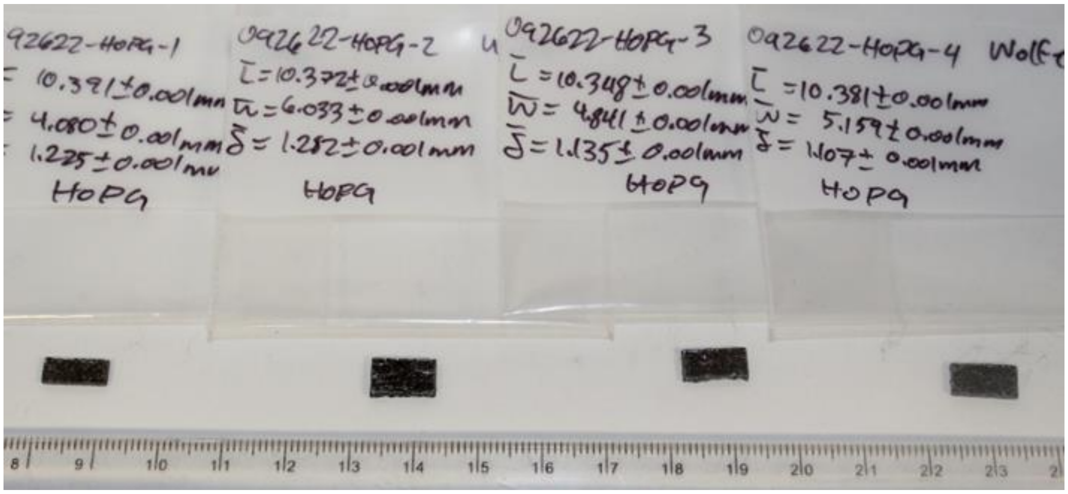

Figure 30. HOPG samples prepared for titanium coating via magnetron sputtering. The top and bottom surfaces are cleaved two times.

Following the successful deposition of the Ti layer on the graphite by magnetron sputtering, samples of HOPG are prepared for titanium coating. 1 cm x 1 cm squares of 2 mm thick YZA grade HOPG are cut in half into two smaller rectangular pieces (Fig. 30). The surfaces of the HOPG samples are then cleaved using a piece of scotch tape to remove the outer graphene layers from the substrate. This process is performed two times on each side of the HOPG samples. The cut and cleaved HOPG samples will be sent to CINT for depositing a Ti layer by magnetron sputtering.

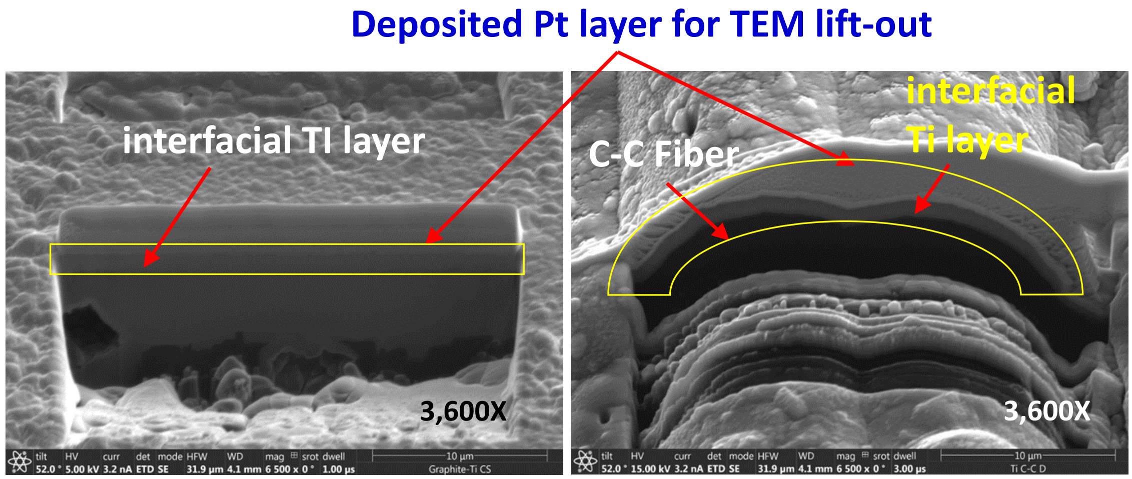

(a) Graphite substrate (b) C-C Composite substrate.

Figure 31:1 SEM images of cut trench on (a) graphite and (b) across a pair of titanium coated carbon-carbon composite longitudinal fibers coated with Ti. The yellow box is placed around the ~ 1.4 µm thick layer of Ti coating. Above that in white is platinum for later sample lift-out for TEM analysis.

Samples of Ti-coated graphite and C-C sample are mounted in the SEM at UNM and imaged to characterize the deposited Ti layer. The focused ion beam (FIB) at the SEM facility is used to cut 30 µm wide trenches through the surface of the coated graphite sample to examine the interface. Figure 31 shows SEM images of the trenched sections on the graphite and C-C composite samples. The Ti coating of the graphite sample in this location is uniform and measured to be approximately 1.4 µm thick (Fig. 31a). The FIB trenched section on the C-C composite is cut across a pair of adjacent carbon fibers. The SEM image shows that the thickness of the Ti layer in this section is also uniform and of the same ~1.4 µm thickness as for the graphite sample (Fig. 31b). Prior to trenching with the FIB, a layer of platinum was deposited on top of the magnetron sputtered Ti layer, which appears as a white layer above the darker gray Ti in the SEM images. This platinum layer will be used for lifting out the cut samples from the Ti-coated graphite and C-C composite for the planned TEM analysis in year 2 to characterize the atomic composition at the interface.

In summary, satisfactory progress has been made in the fabrication of Ti/C-C and Ti/graphite samples for the characterization of the diffusion bonding interface between the materials used in the heat pipe radiator panel. Magnetron sputtering has been used to deposit thin ~ 1.4 µm thick titanium layers onto the surface of samples of graphite and carbon-carbon composites, with the process showing satisfactory results. Samples are being cut for future characterization of the interface using TEM analysis.

9. PLANNED ACTIVITIES

The research planned for years 2 and 3 of the remaining grant period will see the completion of ***Task 1: Design and Thermal and Performance Analysis of Proposed Advanced Lightweight Heat Rejection Radiator Concept, Task 3 – Fabrication of Ti/C Fin Materials,*** and ***Task 4* – Characterization of Ti/C Interfaces,** and the start and conclusion of ***Task 2 – Structural Analysis for Determining C-C Composite Armor Thickness***.

The planned activities for next year are to:

- Improve heat pipe modeling capabilities and performing 3D CFD thermal and thermal-hydraulics analysis of lightweight HP radiator modules and conduct parametric analyses to decrease radiator areal density toward target of ≤ 3.0 kg/m^2
- Perform structural-mechanical and thermal FEA analysis of HP radiator modules and estimate induced structural stresses during launch and assess the effectiveness of the C-C composite armor for 10-year life.
- Deposit Ti onto HOPG substrate and characterize diffusion bonding at interface, before and after outgassing. Also investigate Ti-C diffusion bonds after outgassing in hard vacuum.
- Document and publish results.

10. NASA COLLABORATION

Regular contact is maintained with NASA Research Collaborator Dr. Fernando Reyes Tirado at Marshall Space Flight Center a monthly basis over the course of the project. Monthly research progress Zoom teleconference meetings have been held with Dr. Tirado and other NASA personnel to keep them appraised of the research progress, for dissemination within NASA, discussion, and feedback. These meetings have resulted in valuable discussion of results and stimulated suggestions. These regular meetings are expected to continue throughout the course of the project.

11. ANNUAL TECHNICAL SEMINARS

We have scheduled a seminar at Glenn Research Center in Cleveland, OH on January 11, 2023, at 1 pm EST hosted by Lee Mason, to present the work done to date and solicit comments and feedback. This seminar could be delivered virtually.

Completed *and* Planned Annual Technical Seminars

Award Year	***Date***	***NASA Center***	***Seminar POC***	***Seminar Topic and Comments***
1	1/11/23	GRC	Lee Mason, Associate Chief, Power Division Glenn Research Center	Conceptual Designs and Performance Analyses of Innovative Light-Weight Radiator Panels for Waste Heat Rejection into Space

12. POSTDOCTORAL RESEARCHER(S) / STUDENT(S)

Assistance Type	Number	Roles / Comments
Graduate	2	Graduate students funded in part or entirely by the ESI grant have helped with the C-C and Graphite samples’ preparation for Ti deposition, the characterization of the coated samples, and the modeling and simulation tasks.
Undergraduate	2	Undergraduate students funded by the ESI grant assisted with the upgrade of the vacuum test facility
Other		

13. ACKNOWLEDGEMENTS

We wish to acknowledge the valuable assistance provided by J. Kevin Baldwin at the Center for Integrated Nanotechnologies (CINT) at Los Alamos National Laboratory in performing the magnetron sputtering coating of the prepared C-C composite and graphite samples and for helping the upgrade of the vacuum facilities at UNM-ISNPS. The magnetron sputtering of Ti onto the surfaces of the prepared C-C and graphite samples is performed as part of a 2022 CINT rapid access proposal to UNM-ISNPS (CINT proposal number 2022ARA0038) to support the research on the NASA ESI grant.

This work was performed, in part, at the Center for Integrated Nanotechnologies, an Office of Science User Facility operated for the U.S. Department of Energy (DOE) Office of Science by Los Alamos National Laboratory (Contract 89233218CNA000001) and Sandia National Laboratories (Contract DE-NA-0003525).

We are also grateful for the access to the resources of the High-Performance Computing Center at Idaho National Laboratory, which is supported by the Office of Nuclear Energy of the U.S. Department of Energy and the Nuclear Science User Facilities under Contract No. DE-AC07-05ID14517 and the UNM Center for Advanced Research Computing, supported in part by the National Science Foundation, for providing access to its high-performance computing capabilities.

Nomenclature

A_{an}	Flow area of heat pipe liquid annulus (m^2)
A_v	Heat pipe vapor flow area (m^2)
AMTEC	Alkali Metal Thermal to Electric Conversion
Ar	Argon
C-C	Carbon-Carbon
CBC	Closed Brayton Cycle
CFD	Computational Fluid Dynamics
CINT	Center for Innovative Nanotechnologies
Cs	Cesium
D_c	Heat pipe curvature diameter (m)
D_e	Equivalent diameter (m)
DOE	Department of Energy
ESI	Early Stages Innovation
FEA	Finite Element Analysis
FIB	Focused Ion Beam
FOM	Figure of Merit
FPSE	Free Piston Stirling Engine
h_{fg}	Latent heat of vaporization (J/kg)
HOPG	Highly Oriented Pyrolytic Graphite
HP	Heat Pipe
K	Potassium
L_{cd}	Heat pipe condenser length (m)
L_{hp}	Heat pipe length (m)
LANL	Los Alamos National Laboratory
MW	Molecular weight of working fluid (kg/mol)
NaK	Sodium-Potassium alloy
NASA	National Aeronautics and Space Administration
$P_{cd,0}$	Stagnation pressure in heat pipe condenser (Pa)
$P_{ev,0}$	Stagnation pressure in heat pipe evaporator (Pa)
R_g	Gas constant (J/mol-K)
R_p	Geometric radius of pores in wick (m)
Rb	Rubidium
Q	Heat pipe power throughput (W)
Q_{cap}	Heat pipe capillary limit (W)
Q_{ent}	Heat pipe entrainment limit (W)
Q_s	Heat pipe sonic limit (W)
SEM	Scanning Electron Microscopy

SOA	State-of-the-Art
t_{an}	Width of liquid annulus (m)
$T_{cd,0}$	Heat pipe condenser vapor interface temperature (K)
$T_{ev,0}$	Heat pipe evaporator vapor interface temperature (K)
T_{ex}	NaK-78 exit temperature (K)
T_{in}	NaK-78 inlet temperature (K)
T_s	Module average surface temperature (K)
TE	Thermoelectric
TEM	Transmission Electron Microscopy
Ti	Titanium
TRL	Technology Readiness Level
UNM	University of New Mexico
UNM-ISNPS	University of New Mexico’s Institute for Space and Nuclear Power Studies
W_{ev}	Evaporator width (m)
W_{fin}	HOPG/Ti/C-C fin width (m)
δ_{HOPG}	Fin HOPG thickness (m)
ΔP_l	Liquid pressure loss (Pa)
ΔP_v	Vapor pressure loss (Pa)
ΔT	Module temperature difference (K)
ε	Emissivity
θ	HOPG fillet angle (degrees)
μ_l	Liquid viscosity (Pa-s)
ρ_l	Liquid density (kg/m^3)
σ_l	Liquid surface tension (N/m)

References and Citations

1. Tournier, J.-M., and M. S. El-Genk, "Liquid Metal Loop and Heat Pipes Radiator for Space Reactor Power Systems". *J. Propulsion and Power*, **22**(5), 1117-1134, 2006.
2. NASA Space Technology Mission Directorate, Space Technology Research Grants Program, Early-Stage Innovations Appendix, 80HQTR21NOA01-21ESI-B2, Washington, DC, 2021.
3. Siamidis, J., L.S. Mason, “A Comparison of Coolant Options for Brayton Power Conversion Heat Rejection Systems,” NASA/TM—2006-214121, GRC, Cleveland, OH, 2006.
4. Elliott, J. et al. “Prometheus – Project Lunar Fission Surface Power System Study Report.” NASA Jet Propulsion Laboratory, Pasadena, CA, JPL-982-R66153, 2005.
5. Mason, L., Poston, D., Qualls, L., “System Concepts for Affordable Fission Surface Power.” NASA Glenn Research Center, Cleveland, OH, NASA/TM-2008-215166, 2008.
6. El-Genk, M.S., and J.-M. Tournier, "High Temperature Water Heat Pipes Radiator for a Brayton Space Reactor Power System". Proceedings of Space Technology and Applications International Forum (STAIF-06), AIP Conference Proceedings No. 813, 716-729, 2006.
7. Marriott, A., and T. Fujita, "Evolution of SP-100 System Designs," in Proceedings of the 11th Symposium on Space Nuclear Power and Propulsion, Albuquerque NM, 1994.
8. El-Genk, M.S., and J.-M. Tournier, "Performance Analysis of Potassium Heat Pipes Radiator for HP-STMCs Space Reactor Power System". Proceedings of Space Technology and Applications International Forum (STAIF-2004), AIP No. 699, 793-805, 2004.
9. El-Genk, M.S., Tournier, J.-M., "SAIRS' - Scalable AMTEC Integrated Reactor Space Power System". *J. Progress in Nuclear Energy*, **45**, 25-69, 2004.
10. El-Genk, M.S., Tournier, J.-M., “Performance Comparison of Potassium and Sodium Vapor Anode, Multi-Tube AMTEC Converters,” *J. Energy Conver. & Manag.*, **43**, 1931-1951, 2002.
11. Foust, O.J., Sodium-NaK Engineering Handbook Volume I: Sodium Chemistry and Physical Properties, Science Publishers Inc., New York, NY, 1972.

12. Morscher, G.N. et al., “A simple test to determine the effectiveness of different braze compositions for joining Ti-tubes to C/C composite plates,” *J. Materials Science and Engineering A*, **418**, 19-24, 2006.
13. Cerny, J., G. Morscher, “Adhesive Bonding of Titanium to Carbon-Carbon Composites for Heat Rejection Systems,” in Mechanical Properties and Performance of Engineering Ceramics II: Ceramic Engineering and Science Proceedings, (eds R. Tandon, A. Wereszczak and E. Lara-Curzio). https://doi.org/10.1002/9780470291313.ch12
14. Lan, F.T. et al., “Joining of carbon/carbon composites for nuclear applications,” *Journal of Material Science*, **44**, 3747-3750, 2009.
15. Juhasz, A.J., “High Conductivity Carbon-Carbon Heat Pipes for Light Weight Space Power System Radiators,” NASA/TM-2008-215420, Glenn Research Center, Cleveland, OH, 2008
16. Sheehan, J.E., Buesking, K.W., Sullivan, B.J., “Carbon-Carbon Composites,” *Annu. Rev. Mater. Sci.*, **24**, 19-44, 1994.
17. Grujicic, M. et al., “Hypervelocity impact resistance of reinforced carbon–carbon/carbon–foam thermal protection systems,” *Applied Surface Science*, **252**, 5035-5050, 2006.
18. Klemens, P.G., Pedraza, D.F., “Thermal conductivity of graphite in the basal plane,” *Carbon*, **32**(4), 735-741, 1994.
19. Optigraph GmbH, “HOPG Physical Characteristics,” http://www.optigraph.eu/basics.html, 2011.
20. Xie, W.H. et al., “High velocity impact tests on high temperature carbon-carbon composites,” *Composites Part B*, **98**, 30-38, 2016.
21. El-Genk, M.S., Tournier, J-M., "Uses of Liquid-Metal and Water Heat Pipes in Space Reactor Power Systems". *J. Frontiers in Heat Pipes*, **2**, 3002, 2011.
22. Peterson, G.P., An Introduction to Heat Pipes: Modeling, Testing, and Applications, John Wiley & Sons, New York, NY, 1994.
23. The Mathworks. 2022, Simulink Version 10.1(R2020a), http:/www.mathwors.com
24. Siemens PLM, 2021, STAR-CCM+, http://www.cd-adapco.com/
25. Busse, C.A., “Pressure drop in the vapor phase of long heat pipes,” In IEEE Conf. of Thermionic Conversion Specialists, 391-398, 1967.
26. Shah, R.K., Bhatti, M.S., “Laminar convective heat transfer in ducts” in Handbook of Single-Phase Conductive Heat Transfer, New York, NY, 1987.
27. Sanzi, J.L, Jaworske, D.A, “Heat Pipes and Heat Rejection Component Testing at NASA Glenn Research Center,” Technical Report NASA/TM-2012-217205, Glenn Research Center, Cleveland, OH, 2012.
28. Sanzi, J.L, Jaworske, D.A, Siamidis, J. “Cold Start of a Radiator Equipped with Titanium-Water Heat Pipes,” In 6th International Energy Conversion Eng. Conf. (IECEC), 5749, 2008.
29. Moutis, N.V., et al., “Brazing of carbon-carbon composites to Nimonic alloys,” *J. Mater. Sci*., **45**, 74-81, 2010.
30. Salvo, M, et al., “Joining of Carbon-Carbon Composites for Thermonuclear Fusion Applications,” *J. American Ceramics Soc.*, **80**(1), 206-212, 1997
31. Baldwin, J.K., Mara, N.A., “Physical Vapor Deposition Laboratory,” Center for Integrated Nanotechnologies, Los Alamos, NM, 2016.
32. Diffusion Bonding, Welding Fundamentals and Processes, Vol 6A, ASM Handbook, Editors: T. Lienert, T. Siewert, S. Babu, V. Acoff, ASM International, 2011, 682–689, https://doi.org/10.31399/asm.hb.v06a.a0005612.
33. Gusev, A.I., “Phase equilibria, phases and chemical compounds in the Ti-C system,” *Russian Chemical Reviews*, **71**(6), 439-463, 2002.